Article:
Rashid, F, Hussain, D, Lorinczi, P et al. (1 more author) (2023) The effect of fracturing on permeability in carbonate reservoir rocks. Marine and Petroleum Geology, 152. 106240. ISSN 0264-8172

https://doi.org/10.1016/j.marpetgeo.2023.106240

THE EFFECT OF FRACTURING ON PERMEABILITY IN CARBONATE RESERVOIR ROCKS

F. Rashid[1*], D. Hussein[2], P. Lorinczi[3] and P.W.J. Glover[3]

1-Kurdistan Institution for Strategic Studies and Scientific Research, Sulaimani, Iraq.

2-Geology Department, University of Sulaimani, Iraq.

3-School of Earth and Environment, University of Leeds, UK.

*Author for correspondence, email: fraidoon.rashid@kissr.edu.krd

Abstract

Hydrocarbon flow rates from tight carbonate reservoirs often depend on the distribution and properties of fractures throughout the reservoir interval. Hence, quantification of fracture parameters can contribute to understanding of reservoir characteristics and reservoir potential. In this paper, natural fractures in tight carbonate reservoir rocks of the Upper Cretaceous Shiranish Formation in the Taq Taq field (Kurdistan Region of North Iraq) were examined primarily using core samples, XRMI micro-resistivity image logs and conventional wireline logs, with additional dynamic data from well tests and mud logs. The Shiranish Formation is composed of a variety of limestones and argillaceous limestones with arithmetic mean matrix porosity and geometric mean permeability values of 1.64±0.37% and 0.0223±0.59 mD, respectively. However, fracturing has enhanced the permeability by up to four orders of magnitude above the maximum matrix permeability (1.79±0.59 mD). Hydrocarbons are produced entirely from the fracture network in these rock types in the Taq Taq reservoir. Observed open and partially-open fractures have NE-SW orientations; these are classified as macro-fractures with average aperture of 0.17±0.18 mm, arithmetic mean height of 11.70±45.40 mm and arithmetic mean length of 26.7±32.32 cm, where the uncertainties are standard deviations. Fracture aperture size and fracture height control fracture permeability and fluid flow. However, while fracture frequency has no effect on permeability, fracture distance distribution influences flow rates and hydrocarbon production. The dominant NE-SW trending fractures are more likely to remain open within the NE-SW oriented present day stress field at Taq Taq. Furthermore, the effect of overburden stress on the permeability and production rate was examined in laboratory tests on core plugs by increasing the confining stress during permeability measurements using constant flow rates. It was found that the magnitude of fracture permeability was reduced by 70% by applying 4000 psi of

confining stress. In the reservoir, this effect would be exacerbated by reduced reservoir fluid pressures as a function of production. However, fractures with apertures greater than 0.10 mm are preserved as productive fractures even at high confining pressures and implying that hydraulic fracturing could open existing fractures significantly, enhancing production. This last observation implies that the use of hydraulic fracturing in tight carbonate reservoirs with natural fracturing is likely to be commercially viable.

Key words: Shiranish Formation, Taq Taq field, Kurdistan, Cretaceous, fractured reservoir, permeability, fluid flow, tight carbonates.

1. INTRODUCTION

Carbonate reservoir rocks hold the majority of proven hydrocarbons in global oil and gas fields (Bagrintseva, 2015; Moore and Wade, 2013). Fluids are stored in both matrix porosity and in fractures in carbonate reservoirs, and reservoir quality is controlled both by the original microstructure and by subsequent diagenetic modifications and fracture distribution (Moore and Wade, 2013; Skalinski and Kenter, 2014).

Fractured zones in carbonate rocks result from both regional-scale tectonic activity and diagenetic modifications (Kosari et al., 2017; Ezati et al., 2018). Understanding the nature of fractured carbonate reservoirs is challenging because fractures may be characterized by heterogeneous geometries and connectivity. The evaluation of fracture distributions and fracture properties can help to identify the influence of a fracture network on fluid flow pathways and on production performance (Afsar et al., 2014; Méndez et al., 2020; Rashid et al., 2021).

Permeability in carbonate rocks usually ranges widely in magnitude and exhibits a spatial distribution resulting from lithological variations, diagenetic processes and fracturing of the host rocks (Michie, 2015; Al-Khalifah et al., 2020; Fu et al., 2020; Mohammed Sajed and Glover, 2020). Permeability values in fractured carbonate reservoir rocks are, in general, consistent with fracture parameters including frequency (fracture number per unit length), height, aperture and connectivity (Panza et al., 2016; Menezes, 2020). We infer that a lack of fracture and permeability data from heterogeneous carbonate rocks may have limited previous investigations of permeability variations relevant to fracture parameters and stress variations in productive fractured carbonates.

Most machine learning studies of tight carbonates (e.g., Al-Khalifah et al., 2020 and Glover et al., 2022) have not considered fracturing as a perturbation to permeability prediction or facies clustering. However, advances are being made in the field of quantitative diagenesis, where fracturing is considered to be a cause of, an adjunct to, and a result of fracturing (Rashid et al., 2022; Mohammed

Sajed and Glover, 2020; 2022; Mohammed Sajed et al., 2021). While this paper does not use machine learning, it aims to provide information on fracturing which may allow the effects of fracturing to be built into future machine learning approaches.

In the Zagros fold belt of the Kurdistan Region of northern Iraq, most producing reservoirs are composed of Cretaceous and Cenozoic carbonates (Aqrawi et al., 2010; Rashid et al., 2015a, Hussein et al., 2017; Rashid et al., 2020a). Within the Cretaceous succession in the Kirkuk Embayment, the Kometan and Shiranish Formations form the most important reservoir interval after the Qamchuqa Formation and represent an important exploration target as exemplified by recent discoveries such as the Taq Taq field (Figure 1) (Abdullah et al., 2019; Ghafur, 2020; Ghafur et al., 2020).

This paper focuses on the characterization of fractures in the Upper Cretaceous (Campanian–Maastrichtian) Shiranish Formation in the Taq Taq oil field in Iraqi Kurdistan (Figure 1) using available cores and wireline image logs. The objective was to collect and interpret information about the fracture system in wells TT-05, TT-06 and TT-07 (Figures 1 & 2) in order to evaluate the present-day *in situ* stress regime; and to compare fracture data with dynamic (mud loss and well test) data. The overall purpose was to investigate the influence of fracture parameters on fluid movement and production behavior, and to establish fracture parameters useful for further field development. The results have potential application for the future exploration of tight Cretaceous carbonates elsewhere in northern Iraq and the Zagros fold belt as well as guiding reservoir management decisions in other fractured tight carbonate formations globally. The principal objectives of this study are to understand the impact of the regional stress on the nature and orientation of fracturing throughout the specific intervals of tight carbonate rocks in the Zagros folded zone for predicting the dominant fracture network orientation including natural and artificial fractures and their influence on fluid flow while drilling and production. Consequently, the fracture parameters contribution on the magnitude of the fracture permeability was examined for identifying the most appropriate element of fracture on fluid movement within the fracture pathways.

2. GEOLOGICAL SETTING

The Taq Taq structure is located in the northern part of the Kirkuk Embayment (Figure 1). The structure is an asymmetric, thrust-related, doubly-plunging anticline with a surface extent of 27 km by 11 km, striking NW-SE, i.e. parallel to the main trend of the Zagros fold-and-thrust belt (Figure 2). The field is the largest to have been discovered recently in the Kurdistan Region (Law et al., 2014; Mackertich and Samarrai, 2015). Its producing reservoirs consist of the Eocene Pilaspi Formation and the Cretaceous Shiranish, Kometan and Upper Qamchuqa Formations (Al Shdidi et al., 1995; Garland et al., 2012;

Figure1

Click here to access/download;Figure;Figure 1.tif

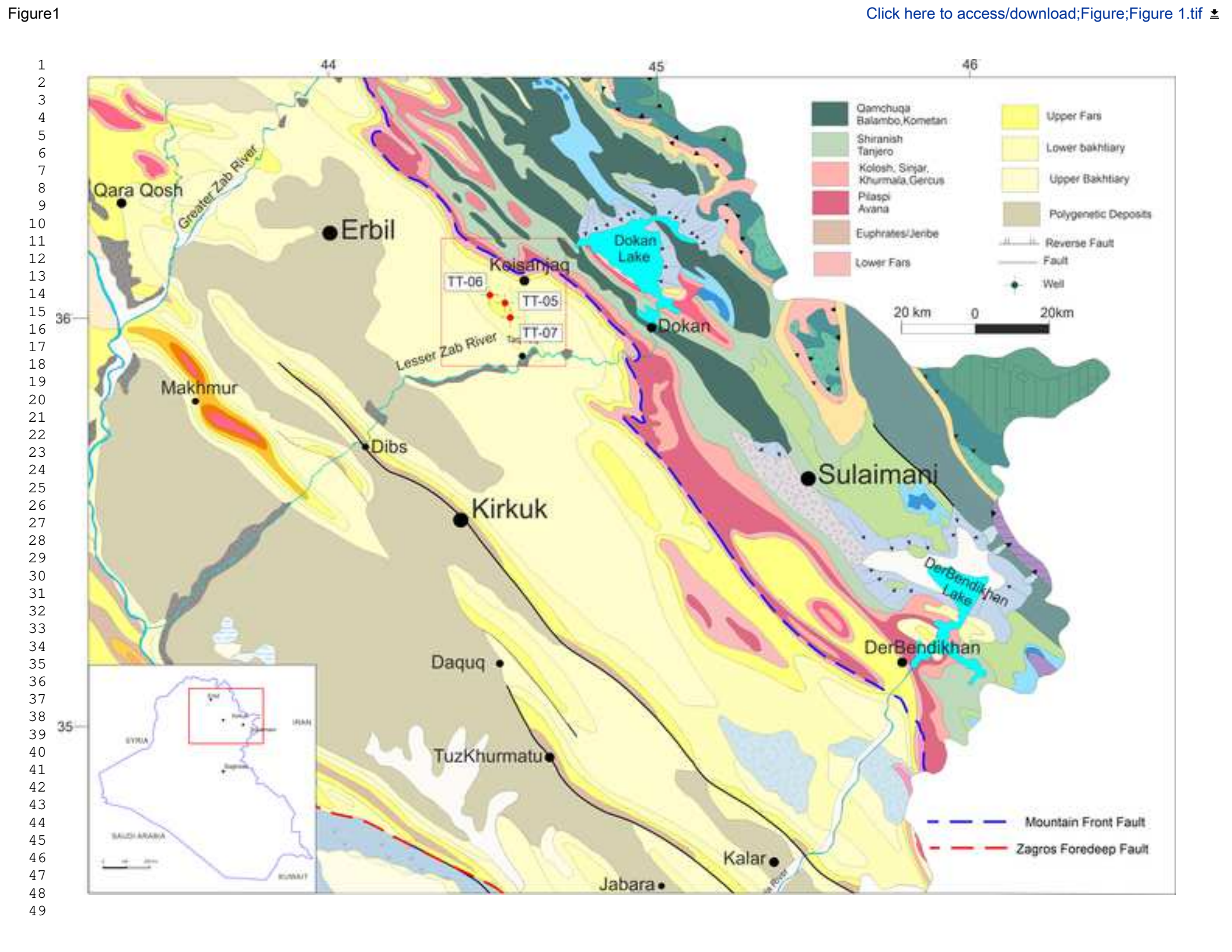

Figure 2

Click here to access/download;Figure;Figure 2.tif

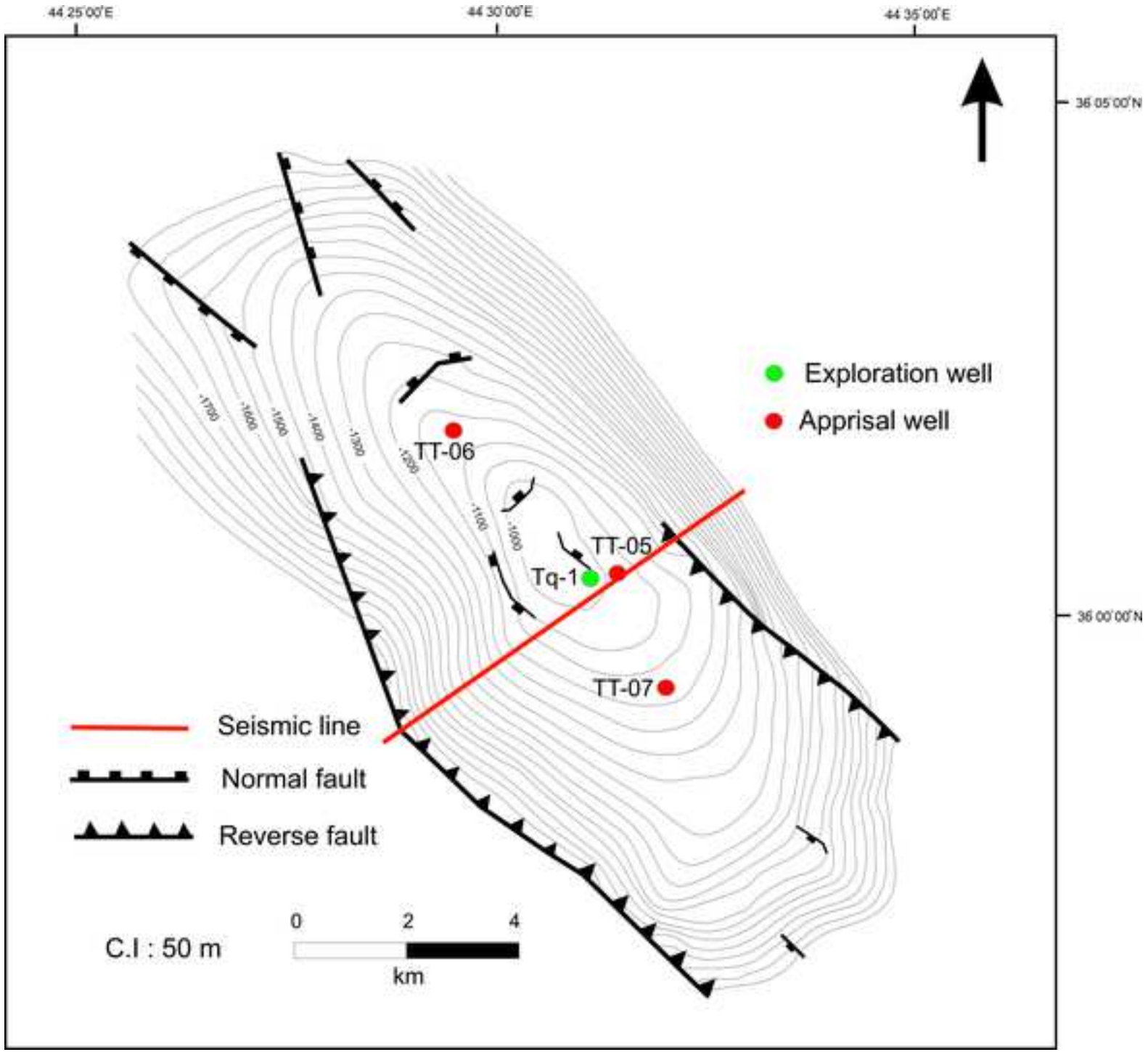

English et al., 2015). The stratigraphic succession in the field is summarized in Figure 3 based on data from drilled wells.

The Taq Taq anticline is developed over a gently NE dipping reverse fault or thrust with some 200 m of throw at Jurassic level on the SW flank of the structure (Figure 4). This thrust terminates upwards within the Pilaspi Formation. A smaller, steeper back-thrust is present on the NE flank of the structure, terminating within the Kolosh Formation. Data from 2D seismic studies also show several smaller-scale faults including a normal fault system parallel to the axis of the anticline, and normal faults were observed in the crestal part of the fold where the radius of curvature is greatest. A horst and graben system has been observed in the Cretaceous succession, including the Kometan and Qamchuqa Formations, running parallel to the fold axis in the central and SE part of the structure. In addition, additional faults affect the shallow section comprising the Lower Fars Formation and overlying succession in the SE part of the structure.

At the Taq Taq field, hydrocarbon accumulations are present in carbonate reservoirs including the Middle-Upper Eocene Pilaspi Formation, the Upper Cretaceous Shiranish and Kometan Formations, and the Middle Cretaceous Qamchuqa Formation (Garland et al., 2010; Mackertich and Samarrai, 2015). These formations have variable reservoir qualities and productivities. The best reservoir characteristics occur in dolomite intervals in the Qamchuqa Formation (Al-Qayim and Rashid, 2012), which contain well-preserved primary and secondary pore types and extensive interconnected fractures. However, high permeabilities in tight limestones of the Kometan and Shiranish Formations show that fracturing has significantly enhanced connectivity in these units, resulting in increased fluid flow (Rashid, 2008; Rashid, 2015). Reservoir quality in the Pilaspi Formations is represented by heterogeneous dolomite intervals with an extensive fracture network (Al-Qayim and Othman, 2012).

The Shiranish Formation is dated as Maastrichtian to latest Campanian (van Bellen et al., 1959). The formation consists of argillaceous limestones overlain by locally dolomitic pelagic marls, and occasional marly limestone beds (Buday, 1980). The upper contact of the Shiranish Formation with the Tanjero Formation is gradational through the interfingering of marlstone beds and is erosional and unconformable with the Sinjar and Kolosh Formations. The lower contact with the Kometan Formation is also unconformable. The formation reaches a thickness of 227.8 m at its type locality at Shiranish Islam in NW Iraqi Kurdistan (van Bellen et al., 1959).

Lithologically, the formation consists of a cyclic intercalation of marls, marly limestones and limestones (Sadooni, 1996; Al-Banna, 2010). The cycles are frequently argillaceous at the base with limited marls and limestones. The cycles become more calcareous in the middle and upper parts of the formation with increasingly thick limestones beds and an overall reduction in the argillaceous content. Rock components are dominantly composed of a micritic matrix with planktonic and

Figure 3

Click here to access/download;Figure;Figure 3.tif

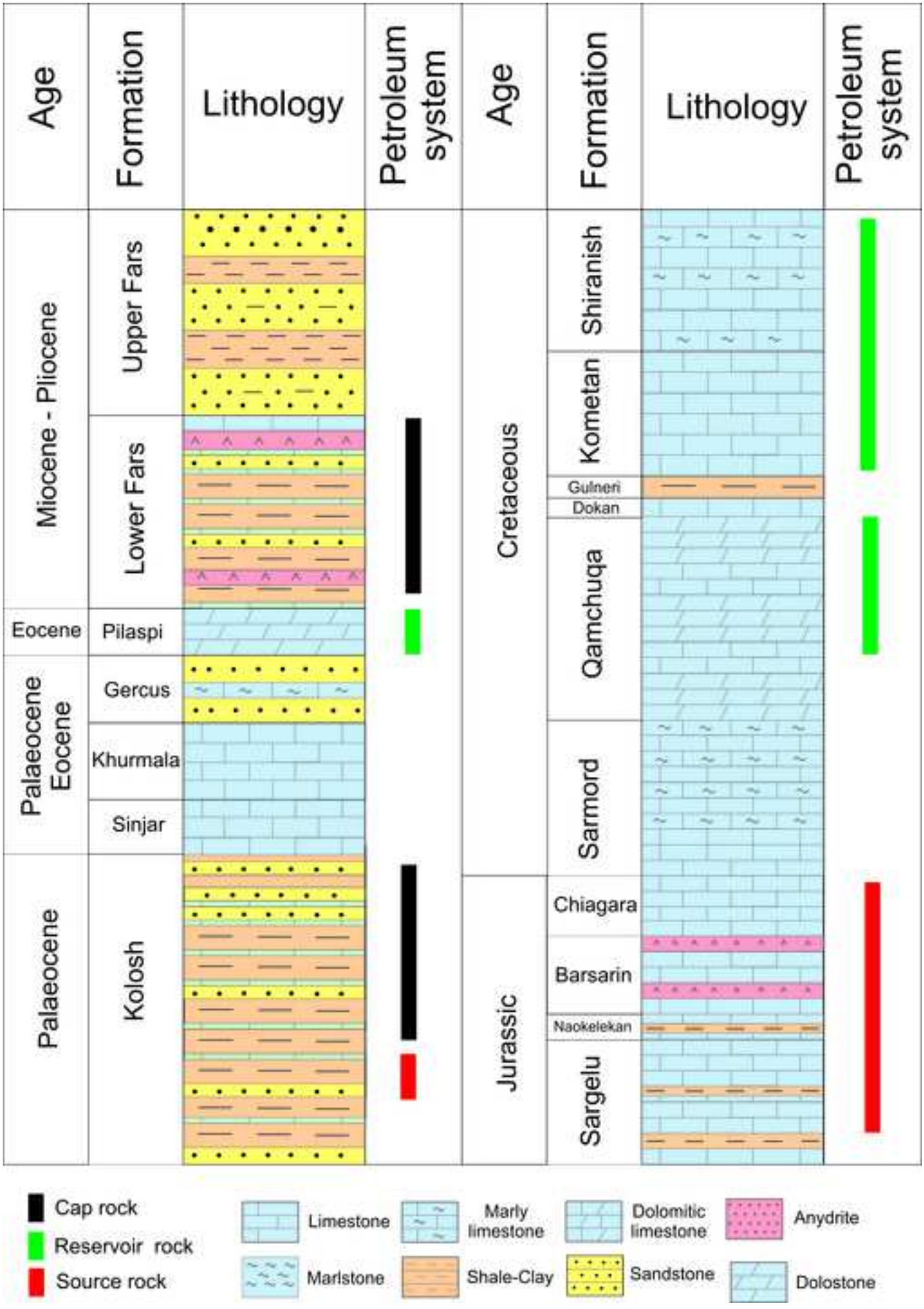

Figure 4

Click here to access/download;Figure;Figure 4.tif

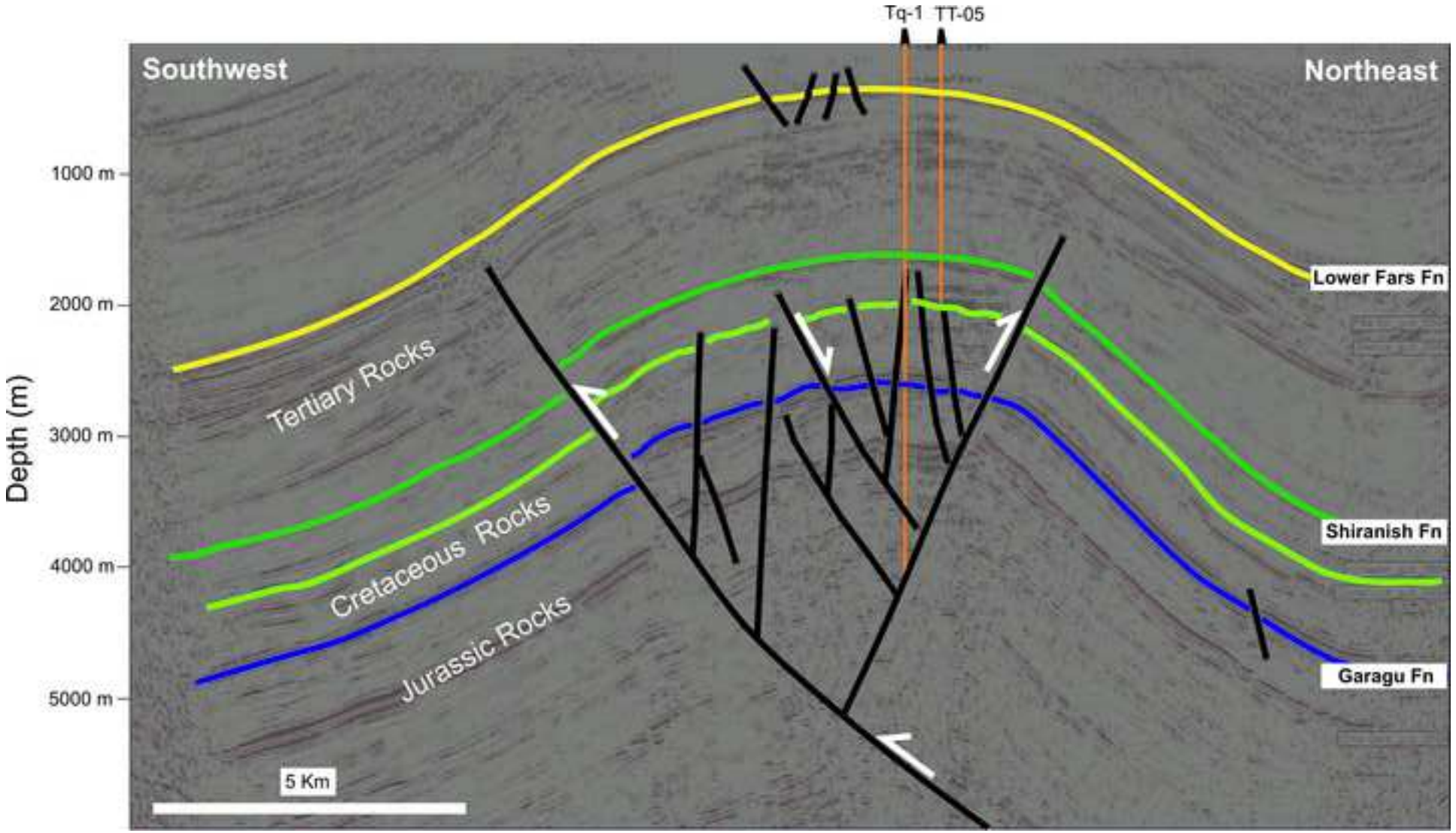

benthonic foraminifera, belemnite fragments and very fine indeterminate skeletal grains (Buday, 1980; Jassim and Goff, 2006; Aqrawi et al., 2010). The formation was deposited in an open marine setting (Aqrawi et al., 2010) as indicated by the dominance of lime wackestones to packstones containing planktonic foraminifera but minor benthonic foraminifera. The occurrence of glauconite suggest tidal reworking in a shallow-marine shelf setting.

3. MATERIALS AND METHODS

The Upper Cretaceous Shiranish Formation was studied at three wells in the Taq Taq oil field: wells TT-05, TT-06 and TT-07 (Figures 1 & 2). Well TT-05 is almost vertical (<1^{o} inclination) and was drilled in the core of the Taq Taq structure about 500 m NE of Well Tq-1 (see Figure 2). The appraisal and development Well TT-06 penetrated the Cretaceous succession on the northern slope of the Taq Taq structure. Well TT-07 is a deviated appraisal and production well drilled on the southern slope of the anticline, about 2 km SE of Well Tq-1 (Figure 2) along the axis of the Taq Taq structure. The well attained an inclination in the Upper Qamchuqa reservoir of up to 17^{o}. Cored intervals comprising 24 m of carbonate rock were collected from three cores from the Shiranish Formation including 18.0 m of core from Well TT-05 (core numbers 1 and 2) and 6.0 m of core from Well TT-06 (Core Number 1) (Figure 5, Table 1). Ditch cuttings were collected with a frequency of one sample per 2 m from the Shiranish Formation in the three wells. Conventional wireline logs together with micro-resistivity (XRMI) image logs were also acquired. Other contextual downhole data included lithology logs, mud log reports, drill stem test (DST) and repeat formation tester (RFT) data (Table 1).

The core and cuttings samples of the Shiranish Formation were studied and sedimentological features including lithology, color, argillaceous content and hardness were recorded together with fractures, oil staining and visible pores. These data combined with data from petrophysical logs and micro-resistivity image logs was used as an integrated dataset for the interpretation of non-cored and total loss intervals in the three wells.

Ten samples were selected for thin-section petrography from available core samples and cuttings. The samples were impregnated with a fluorescent blue-dyed resin (Rosales et al., 2018) prior to preparation for pore type identification. The same samples were also stained for calcite and dolomite identification (Dickson, 1965; 1966). Thin sections were made from the impregnated samples using standard procedures and were subsequently studied under transmitted polarized light with a petrographic microscope. Rock textures were analyzed (Dunham, 1962) together with sample mineralogy, pore types and cement fills, and depositional environments were interpreted according to Flugel (2004).

Table 1

Materials	Well TT-05	Well TT-06	Well TT-07
Rock core samples	18 m	6 m	-
Drilling cutting samples	165	140	125
Conventional log	Natural gamma ray (GR), Porosity logs (BHC, RHOB, NPHI), Resistivity logs (LLD, LLS, MSFL)	Natural gamma ray (GR), Porosity logs (BHC, RHOB, NPHI) , Resistivity logs (LLD, LLS, MSFL)	Natural gamma ray (GR), Porosity logs (BHC, RHOB, NPHI), Resistivity logs (LLD, LLS, MSFL)
Borehole Image log	X-tended Range Micro Imager (XRMI)	X-tended Range Micro Imager (XRMI)	X-tended Range Micro Imager (XRMI)
Dynamic data	Well tests Fluid loss data	Well tests Fluid loss data	Well tests Fluid loss data

Figure 5

Click here to access/download;Figure;Figure 5.tif

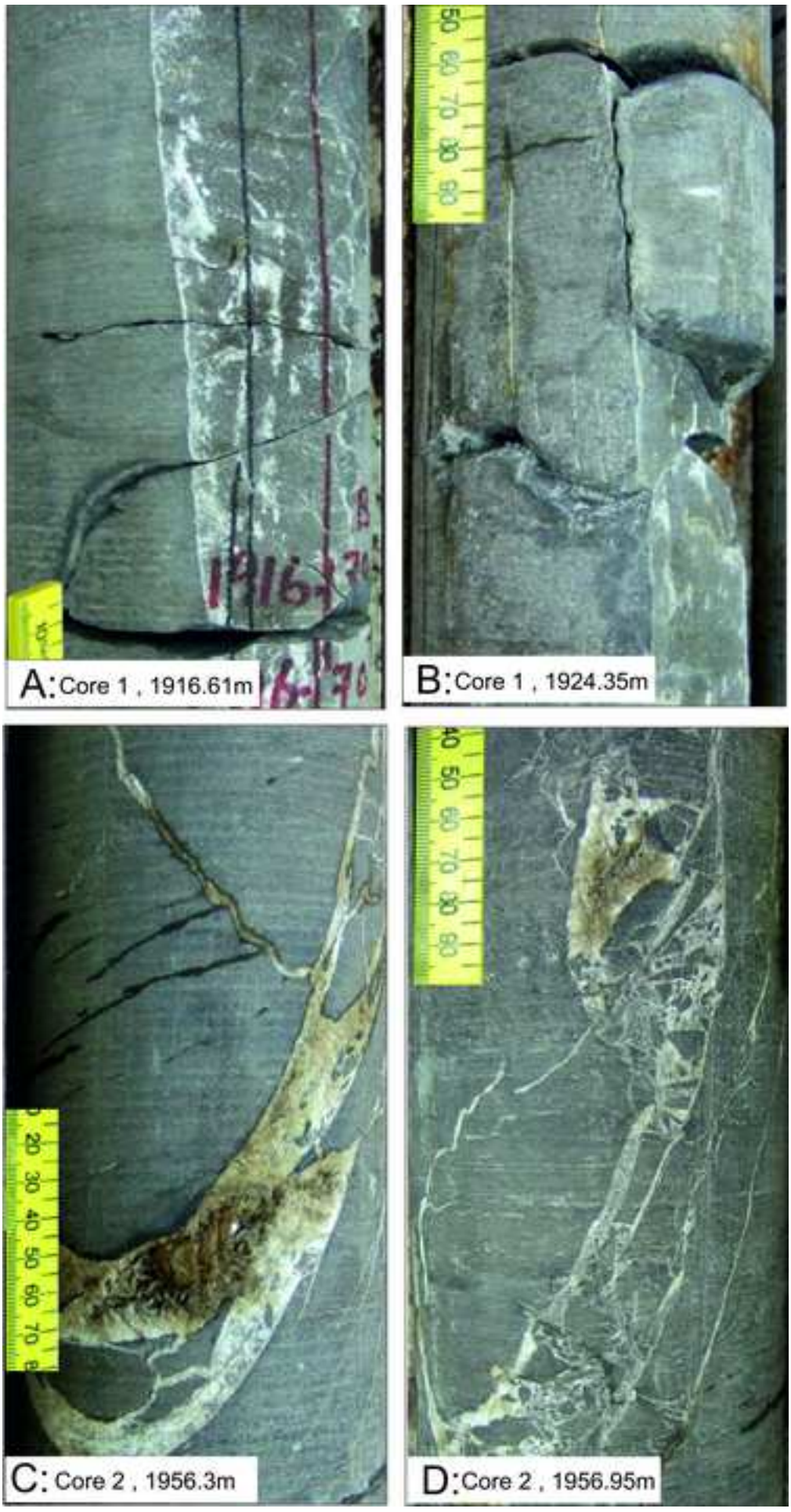

Core fracture measurement was carried out as soon as the cores were removed from the core barrels and prior to any slabbing or sampling. The individual core pieces were fitted back together carefully and then a datum line was ruled along the length of each core, from which the orientation of the fractures would be measured. The apparent dip angle and direction relative to the reference line was recorded for each fracture, as well as the fracture type, length, aperture, fill, height and frequency (fracture length, aperture and height are defined in Figure 6). The collected data was initially oriented with respect to the datum line and then restored in the real geographic position in a subsequent stage. A database of all quantifiable fracture parameters has been complied digitally on Excel spreadsheets.

3.1 Image logs

The CNLC X-tended Range Micro Image (XRMI) tool is a water-based mud micro-resistivity image tool which consists of pads mounted on six independently articulated arms with 25 buttons in each pad. Data processing (depth speed correction) was undertaken by the service companies, and depth control issues were encountered during logging probably related to cable stretch. Variable depth shifts were applied to the image logs to depth match the provided wireline data (the wireline GR curve was used as a reference log). The raw data contained relevant Pad-1 azimuth, hole orientation and borehole caliper data necessary for image orientation and interpretation purposes.

The image logs from the wells studied were of reasonably good quality, but locally were of poor quality due to borehole enlargement (washouts, breakouts) or the presence of heavily fractured zones, especially in the Shiranish intervals. The XRMI images were interpreted over the cored intervals, and a careful search was made for features that could be seen in both the cores and the XRMI images. The core log was then placed alongside the XRMI images at the same scale and other features were noted to match across, confirming the correct core to log correlation.

Interpretation of the processed images was undertaken using Well Cad® 3.2 software from Rockware, whose functionality allows the user to manually adjust the data normalization and data scaling options in order to maximize the detail resolved in the image log data. Hand-picked orientations were calculated for all bedding surfaces and tectonic features observed in the images. The image logs were analyzed for fracture characteristics and distributions and also to calibrate image features against core results available from wells TT-05 and TT-06 in order to establish a unified fracture terminology scheme that could be related to the core observations and extended outside the cored intervals. The azimuth of borehole breakout and tensile axial fractures was obtained by fitting a vertical sine wave through the center of the image feature. More advanced fittings that can account for non-sinusoidal traces caused by non-planar features (Glover and Bormann, 2007) were not available in the analysis software. Consequently, it is an assumption of this work that fractures are

Figure 6

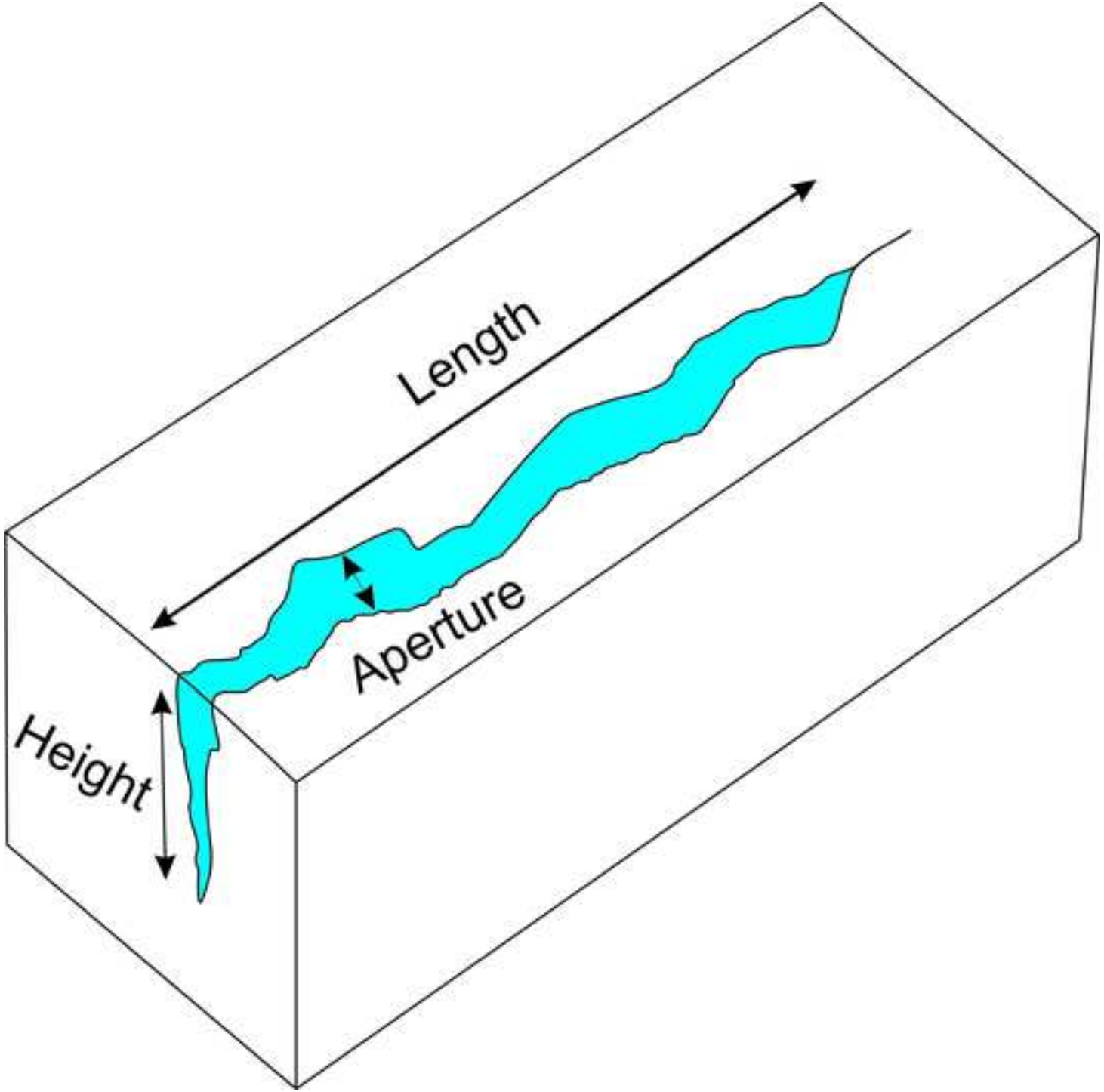

planar at the scale of borehole section. It should also be noted that we note from core analysis that most fractures have irregular surfaces even if they are quasi-planar at larger scales.

3.2 Fracture type and measurements

Fracture measurements (Figure 6) and analysis were performed on Core 1 and Core 2 from Well TT-05 and Core 1 from Well TT-06 (Figure 5). The fracture aperture was measured from the arithmetic mean of the opening part of the fracture surface (effective aperture) using a profile gauge. Fracture height was identified from the average height of a single fracture. The length of both sides of a fracture through a core sample were measured. Values of the length of fractures in each core sample were then achieved bearing in mind the appearance and terminations of individual fractures.

We note that many of the measured properties of fractures (length, height, nodal distance etc.) scale fractally and hence follow a power law (Ortega et al., 2006). For these properties the arithmetic means used in this work are unreliable if taken over a large range of scales such as at an exposure. The more restricted scale range of core measurements or wireline logs which concern us in this work ensures that an arithmetic mean is approximately valid.

Fracture types included open, partially-open and totally filled (cemented) fractures. Fracture parameters including aperture, length and height, frequency per unit length, and orientation were recorded, and measured data were analyzed statistically using Dips® 6.0 software from Rocscience.

Although occasional microfractures were observed in thin sections, the data from these was not included in the data presented in the paper as it was thought that their observation was not sufficiently representative to be statistically valid. No faults are included in the data.

Volumetric intensity estimations (P_{32}) (Dershowitz and Herda, 1992) were not calculated in this work as we prefer to describe the observed fractures rather than predict some value for their frequency. Linear and volumetric intensity estimations may follow in a subsequent publication.

3.3 Conventional petrophysical measurements

Conventional petrophysical measurements, that were made on non-fractured core intervals, included matrix porosity and matrix permeability. The plug samples were drilled horizontally with no considered azimuth from available core samples. Porosity was measured at room temperature and atmospheric pressure on 2.5-inch diameter plugs using a helium gas expansion method (Allshorn et al., 2019). The matrix porosity was measured for 62 plug samples in total; 42 samples from Well TT-05 and 20 samples from Well TT-06. Permeability was measured using a steady-state helium gas permeameter at ambient pressures (Rushing et al., 2004). For each sample, several measurements were performed with the application of different gas inlet pressure (Tanikawa and Shimamoto, 2009).

The results were then corrected for the Klinkenberg effect (Donaldson and Tiab, 2004). In total, 46 plug samples were used for calculating the matrix permeability, 34 samples from Well TT-05 and 12 samples from Well TT-06.

Fracture porosity and permeability were calculated from naturally-formed fractures within the available core intervals. The length, effective aperture, width (height) and frequency were measured for particular fractures to calculate fracture porosity and absolute permeability using the cubic law technique (equations 1 and 2 below; after Witherspoon et al., 1980; Ranjith and Viete, 2011). Fracture parameters including the aperture, length and height of individual fractures within a 1 m^3 core were converted into fracture pore volume; the pore volume was then divided by the apparent bulk core volume to obtain the fracture porosity. The fracture permeability was calculated using the effective aperture of a singular fracture cubed and assuming the fluid flow was laminar through a constant distance between the fracture aperture (Yu et al., 2020). However, the magnitude of estimated fracture permeability using cubic law usually gives overly high permeabilities for at least two reasons. The first is that the fracture aperture and effective fracture length are typically overestimated. The second is that the hydraulic aperture is less than the physical aperture of the fracture due to the roughness of the fracture surfaces (Glover and Hayashi, 1997). These issues are discussed further towards the end of this paper.

The fracture porosity was calculated using

$$\phi = \frac{V_f}{V_B}, \tag{1}$$

where ϕ = fracture porosity, V_f is fracture volume (m^3) and V_B is bulk core volume (m^3), while the permeability was calculated using

$$k = \frac{A^3}{12L}, \tag{2}$$

where k= permeability (m^2), A = fracture aperture (m) and L= fracture length (m). Permeability in millidarcies can be obtained from the conversion: 1 mD = 9.869e-16 m^2.

4. RESULTS

4.1 Stratigraphy

The drilled thickness of the Shiranish Formation is about 334 m in the crest of the Taq Taq anticline at Well TT-05, 296 m in the northwest at Well TT-06, and 250 m in the southeast at Well TT-07. Figure 7 shows that the formation is predominantly carbonate with occasional marly, argillaceous and glauconitic beds at all three wells, while the electrical log data for TT-05 shows a separation between the shallow (LLS) and deep (LLD) resistivity log readings which is indicative of the presence of hydrocarbons, especially for the bottom half of the formation.

At the Taq Taq oil field, the formation is composed of light to olive grey, argillaceous and marly limestones with local shale and dolomitic limestone beds. Limestone textures are dominated by mudstones to planktonic foraminiferal wackestone/packstones (Figure 8A-C). Matrix material consists of argillaceous lime mud, and skeletal grains include abundant planktonic foraminifera and less common benthonic foraminifera and calcispheres with rare indeterminate skeletal debris. The base of the formation is characterized by prominent glauconite-rich horizons enriched with reworked intraclasts. Glauconite grains are up to 500 μm in diameter (Figure 8B), and other grains present include planktonic foraminifera, phosphate nodules and detrital quartz. Overall, macrofabrics range from apparently homogeneous to intensively bioturbated, and in places bioturbation has destroyed the original depositional texture.

Very few open pores were observed in core and cuttings samples, in thin sections or in photomicrographs. Primary intragranular pores within foraminiferal chambers were almost completely cemented by blocky, slightly ferroan calcite. The only preserved primary porosity within the studied intervals consisted of nanoscale intercrystalline pores. However, fracture-related pores of variable sizes were observed (Figure 8D) and were present as isolated vugs or as more continuous interconnected linear features.

4.2 Fractures

Core samples and image data showed both natural and drilling-induced fracture types. Natural fractures were open, partially open (i.e., partially mineralized) or fully cemented (i.e., veins). In this study, only naturally formed fractures that had contributed to fluid flow and hydrocarbon production were analyzed. Fractures induced by drilling or coring were distinguished from natural fractures during the core examination using established guidelines given by Kulander et al. (1990); in image logs, the fractures were differentiated following Prioul et al. (2007) and Lai et al. (2018).

Well TT-05 contained 89 natural, open and partially-open fractures in the 18 m cored section, whereas only four natural fractures were recorded from the cored section (9 m) of Well TT-06. Natural

Figure 7

Click here to access/download;Figure;Figure 7.tif

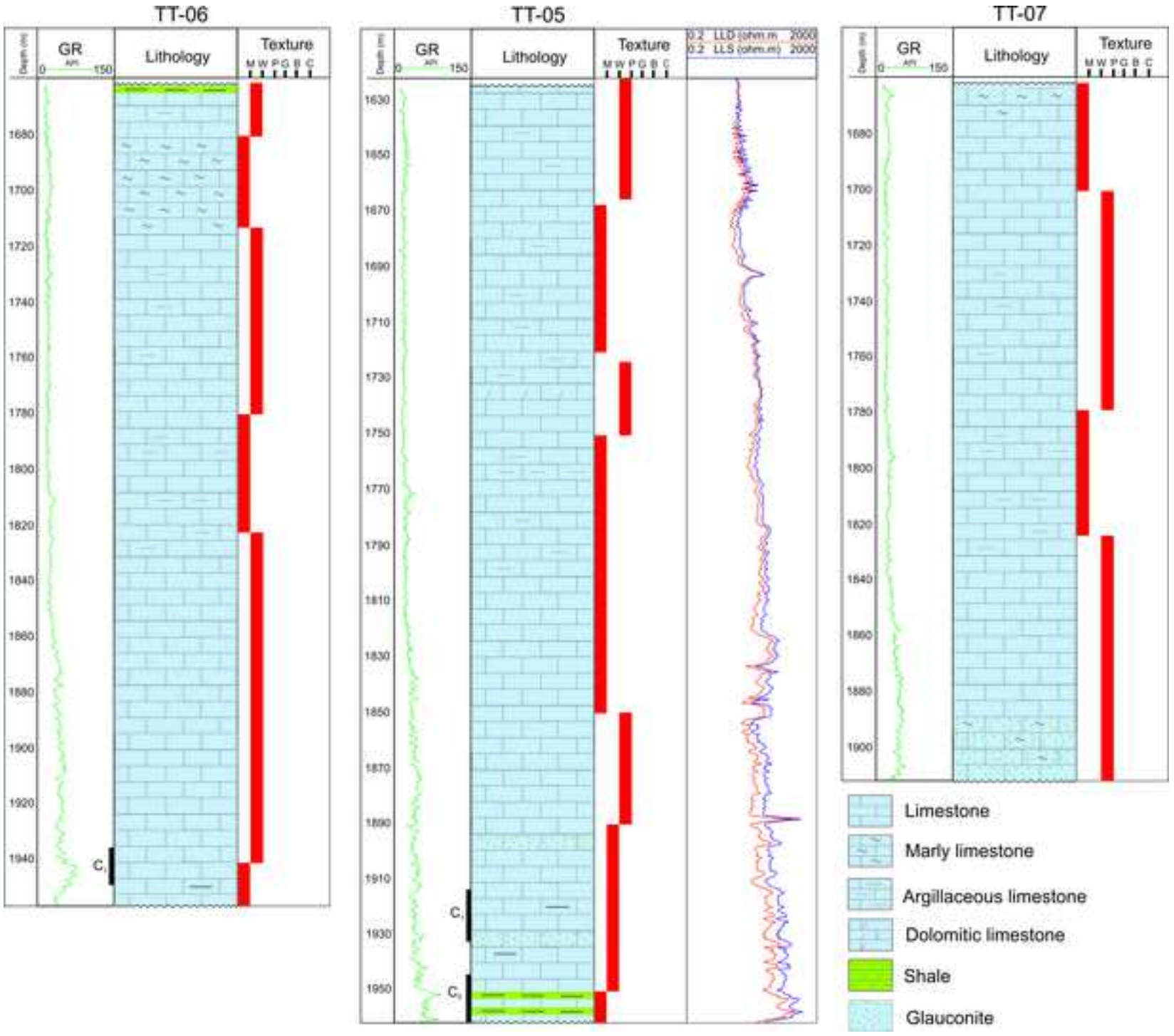

Figure 8

Click here to access/download;Figure;Figure 8 .tif

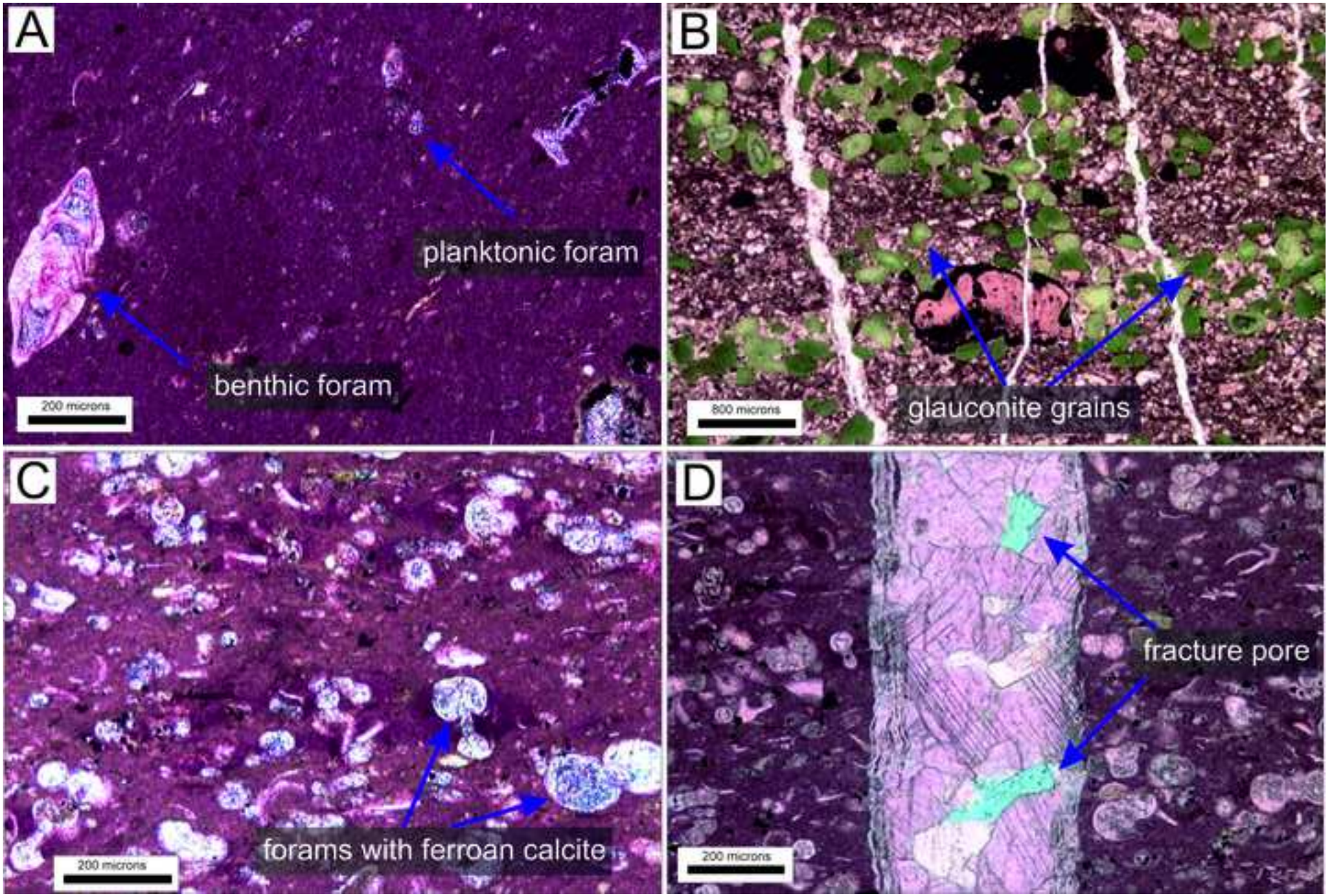

fractures were also recorded from XRMI micro-resistivity image data; 35 fractures in Well TT-05, 80 fractures in Well TT-06, and 50 fractures in Well TT-07.

In addition to natural fractures, numerous induced fractures were observed throughout the studied intervals. In total, 216 induced fractures from the XRMI micro-resistivity image logs and four induced fractures from the core intervals were investigated. The ratio of fracture identification in cores and image logs was high, about 4:1. The observed fractures are four times as many fractures in the core as in the image log for the same section throughout the studied intervals. Variation in the observation of fractures in cores and logs was caused by the poor fracture detection ability of the XRMI image tool and the extensive distribution of induced fractures throughout the drilled intervals. Open and partially open fractures in the core samples (Figure 5A and 5B) had variable apertures ranging from 0.013 mm to 10 mm with low aperture values occurring most frequently (Figure 9A). Fracture length was also variable, ranging between 3.0 cm and 260 cm (Figure 9B). The arithmetic mean of fracture length was 27.0±32.3 cm. Please note that throughout this paper the uncertainties expressed are the standard deviation of all measurements used in the arithmetic mean calculation, unless described as otherwise. The large standard deviation in the fracture length indicates both that there is a very wide range of fracture lengths present, and that the distribution is not Gaussian. Fracture height varied from 0.10 mm to a maximum of 280 mm in fault type fractures, with an average of 11.70±45.40 mm (Figure 9C). The dominant fracture set, derived from the data obtained from core observations, had a ENE-WSW strike (75±5^{o}), which is consistent with maximum principal horizontal stress data from the latest edition of the World Stress Map (Heidbach et al., 2018), and with dips ranging from 39° to 90° with a mean dip of 75° and a quasi-vertical modal dip (>85°) (Figure 10A).

A number of small-scale faults and associated brecciated intervals were identified in the core samples, including 28 different sizes of fault planes. Fault zones and brecciated intervals at 1945 m and between 1952 m and 1958 m were observed in Well TT-05 (Figures 5C-D). Furthermore, low angle bedding plane slip surfaces were also commonly observed in the argillaceous limestones of the Shiranish Formation. The fault planes had lengths ranging from 4 cm to 260 cm (arithmetic mean 33.25±49.57 cm) with an arithmetic mean aperture of 0.10 mm, although an aperture of 80 mm was recorded in an oblique slip fault. Faults measured in the cores showed a predominant ENE-WSW trend (75±10^{o}), which is consistent with maximum principal horizontal stress data from the latest edition of the World Stress Map (Heidbach et al., 2018), as well as a minor SSW-NNE component (15±5^{o}). These faults have an arithmetic mean dip of 50° and a modal value between 60° and 65° (Figure 10B).

4.3 Image logs

Figure 9

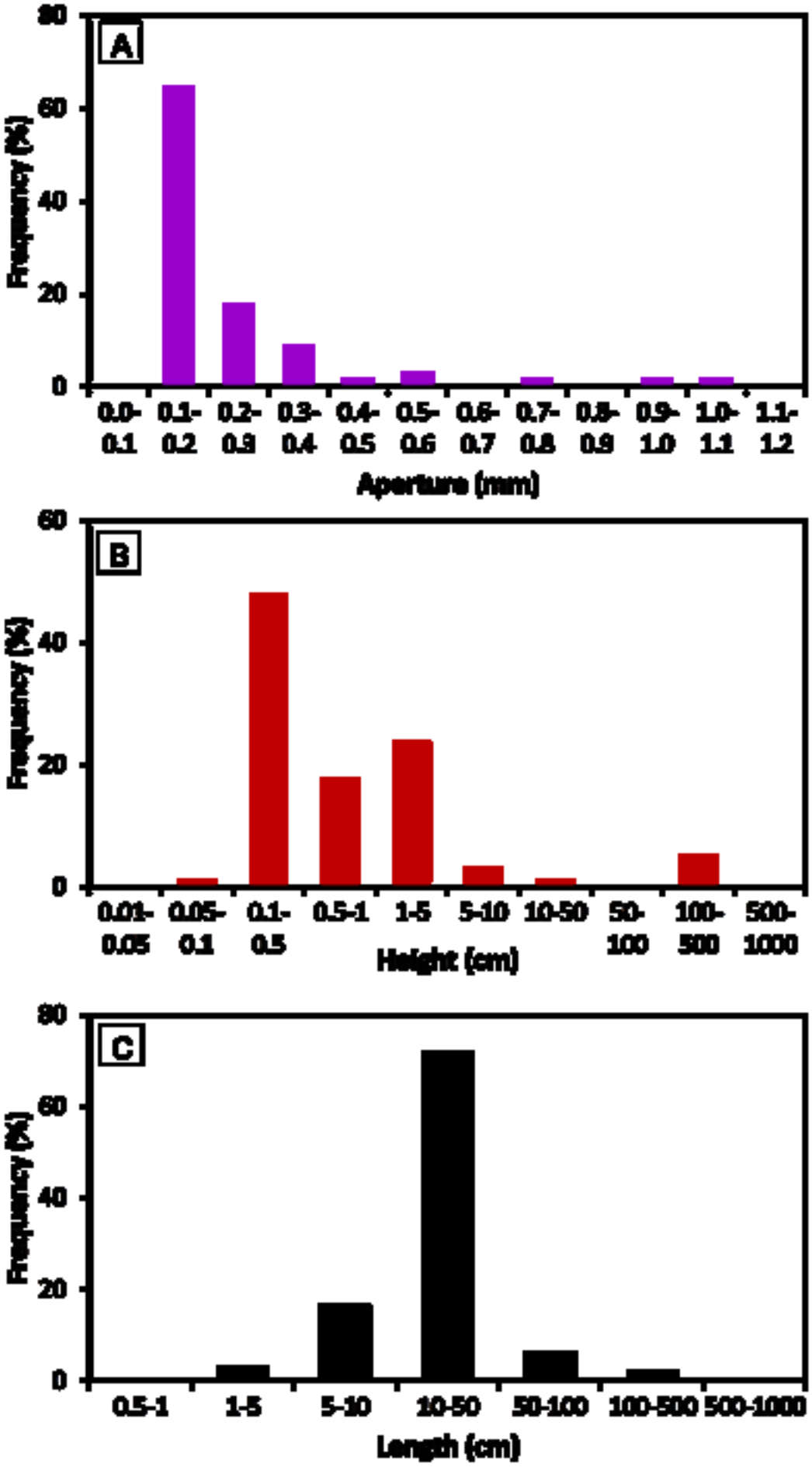

Figure 10

Click here to access/download;Figure;Figure 10.tif

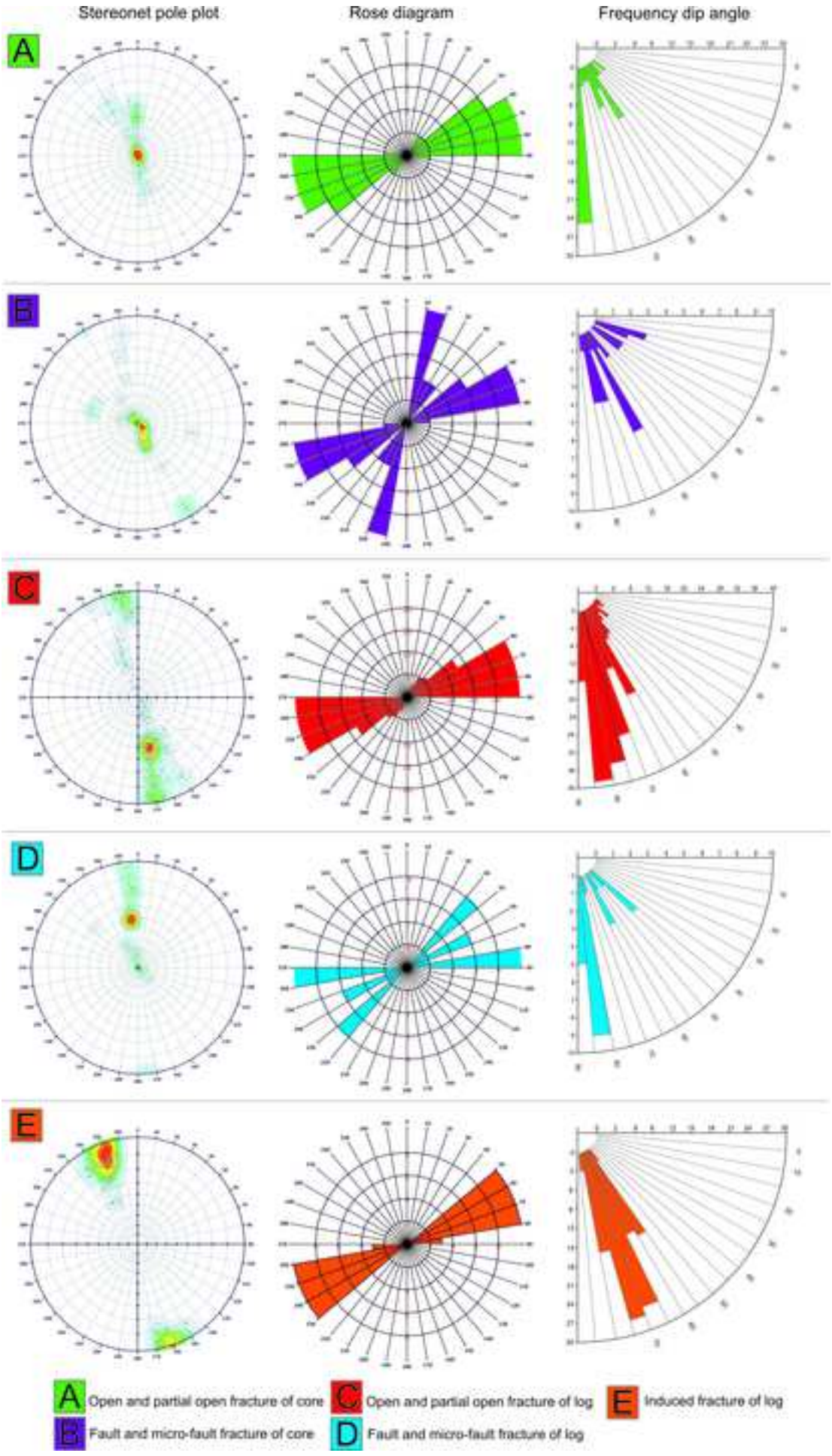

The results of fracture analysis from the image logs were very similar to those from the core observations. In total, 165 open and partially-open fracture types were recorded from the analysed image logs, some of which are shown in Figure 11 with annotations. The fractures in general strike ENE-WSW (75±5°), which is extremely similar to the field data (Figure 10A) and also consistent with maximum principal horizontal stress data from the latest edition of the World Stress Map (Heidbach et al., 2018). These data have dip angles ranging from 21° to 90° (arithmetic mean 72° and a modal value between 80° and 85°) (Figure 10C), which is also consistent with the core-derived values in Figure 10A.

Sinusoidal features in the image logs with different resistivity and obvious displacement across bedding were identified as faults. These features are especially common at depths of 1824- 1831 m and 1915 - 1934 m in Well TT-05, at 1776 m, 1813 m, 1830 m and 1843 m in Well TT-06, and at 1700 m and 1894 m in Well TT-07. The faults strike ENE-WSW (65±25°), which is also consistent with maximum principal horizontal stress data from the latest edition of the World Stress Map (Heidbach et al., 2018) and the core data (Figure 10C), and also have similar dips to those obtained from the core data. The image analysis indicated an arithmetic mean dip angle of 73° but a modal value between 80° and 85° (Figure 10D).

Induced/enhanced fractures were also observed on the XRMI micro-resistivity images in the Shiranish Formation. These are partially open to totally open (conductive) features with a limited extent in the images and were interpreted to have been formed as a result of pressuring due to drilling mud (Sheng et al., 2019; Michael and Gupta, 2020). Induced fractures were locally abundant, especially from 1780 m and below in Well TT-07 (Figure 11) and were consistently oriented ENE-WSW. Dip angles ranged between 51° and 82° with an arithmetic mean of 68° and a modal value between 70° and 75° (Figure 10E).

The similarity between both the dip and strike of the induced fractures with both core and wireline-derived dips and strikes from existing fractures and faults as well as the direction of maximum principal horizontal stress from the world stress map data indicates that all the data is self-consistent and that the stress regime in the region has not changed appreciably since fracturing was active (i.e., within the last 25 Ma).

The directional data in this study seems to be consistent with values of the direction of maximum principal horizontal stress from the world stress map data for reservoirs in all of Iraq and Iran, and probably for most of Saudi Arabia, although here the world stress map data is sparse and individual sources must be sought. The direction of maximum principal horizontal stress over the whole of this area is primarily controlled by the opening of the Red Sea rift, which spreads at a rate of about 10

Figure 11

Click here to access/download;Figure;Figure 11 .tif

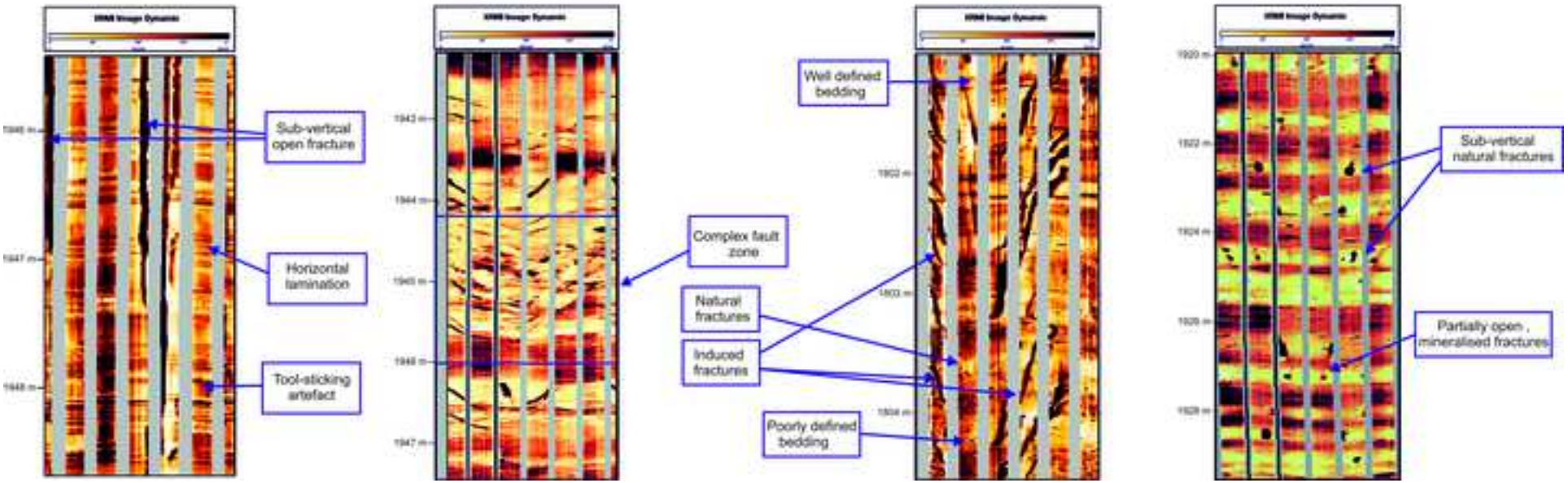

mm/yr at its northernmost extremity to about 16 mm/yr at its southernmost point (Chu and Gordon, 1998), opening in the ENE-WSW direction.

4.4 Porosity and permeability

Statistical data for measured porosity and permeability are presented in Table 2. Measured matrix porosity of plug samples of the Shiranish Formation varied from 0.10% to 11.07% with a geometric mean of 1.64 ±0.37% (Figure 12A). The matrix permeability for the limestone samples analyzed varied from 0.010 mD to 1.79 mD with a geometric mean of 0.0223 ±0.59 mD (Figure 12B; Table 2).

Fracture porosity and permeability obtained from natural fractures in the available core samples differed from measured matrix porosity and Klinkenberg-corrected gas permeability. Fracture porosity ranged from 0.0039% to 0.42% with a geometric mean of 0.038±0.48%. Fracture-related permeability was significantly enhanced, ranging from 0.14 mD to 4.6 $\times 10^4$ mD with a geometric mean of 28.23±1.10 mD. This represents an enhancement of permeability caused by fractures that is at least 1 order of magnitude and reaches four orders of magnitude for the highest permeability samples. The poroperm characteristics and interplay between permeability and fracture parameters will both be presented later in the discussion.

4.5 Dynamic data

Drill stem tests (DSTs) of the Shiranish Formation were run in wells TT-05, TT-06 and TT-07 for fluid recovery together with a repeat formation tester (RFT) for pressure measurement. Completion intervals in Well TT-05 achieved excellent productivity which indicates fracture flow (rather than matrix flow), specifically in the upper part of the drilled intervals. Production from the tested intervals, including the Shiranish Formation at 1665-1770 m and 1830-1865 m, has the potential to exceed 12,660 barrels per day of oil.

In Well TT-06, the Shiranish interval (1658-1681 m) was tested separately and flowed at an aggregate rate of 15,380 barrels of oil per day. The test results in Well TT-07 provided an oil flow rate of 10,240 barrels per day from the Cretaceous succession including the Shiranish Formation interval (1723-1900 m). Furthermore, several total losses were recorded while drilling the Shiranish Formation, including at 1850-1854 m in Well TT-05, and extensive drilling fluid losses were recorded at depths of 1810 m and 1938 m in Well TT-06. These test data are consistent with the calculated fracture permeabilities presented above.

Table (2)

Matrix elements	**Measured Porosity (%)**	**Measured Permeability (mD)**
Lowest	0.10	0.010
Highest	11.07	1.79
Arithmetic mean	1.64	0.1029
Geometric mean	1.09	0.0223
Standard deviation	0.37	0.59
Fracture elements	**Calculated Porosity (%)**	**Calculated Permeability (mD)**
Lowest	0.0039	0.14
Highest	0.42	4.64×10^{4}
Arithmetic mean	0.038	1.46×10^{3}
Geometric mean	0.000194	28.23
Standard deviation	0.48	1.10

Figure 12

Click here to access/download;Figure;Figure 12 .tif

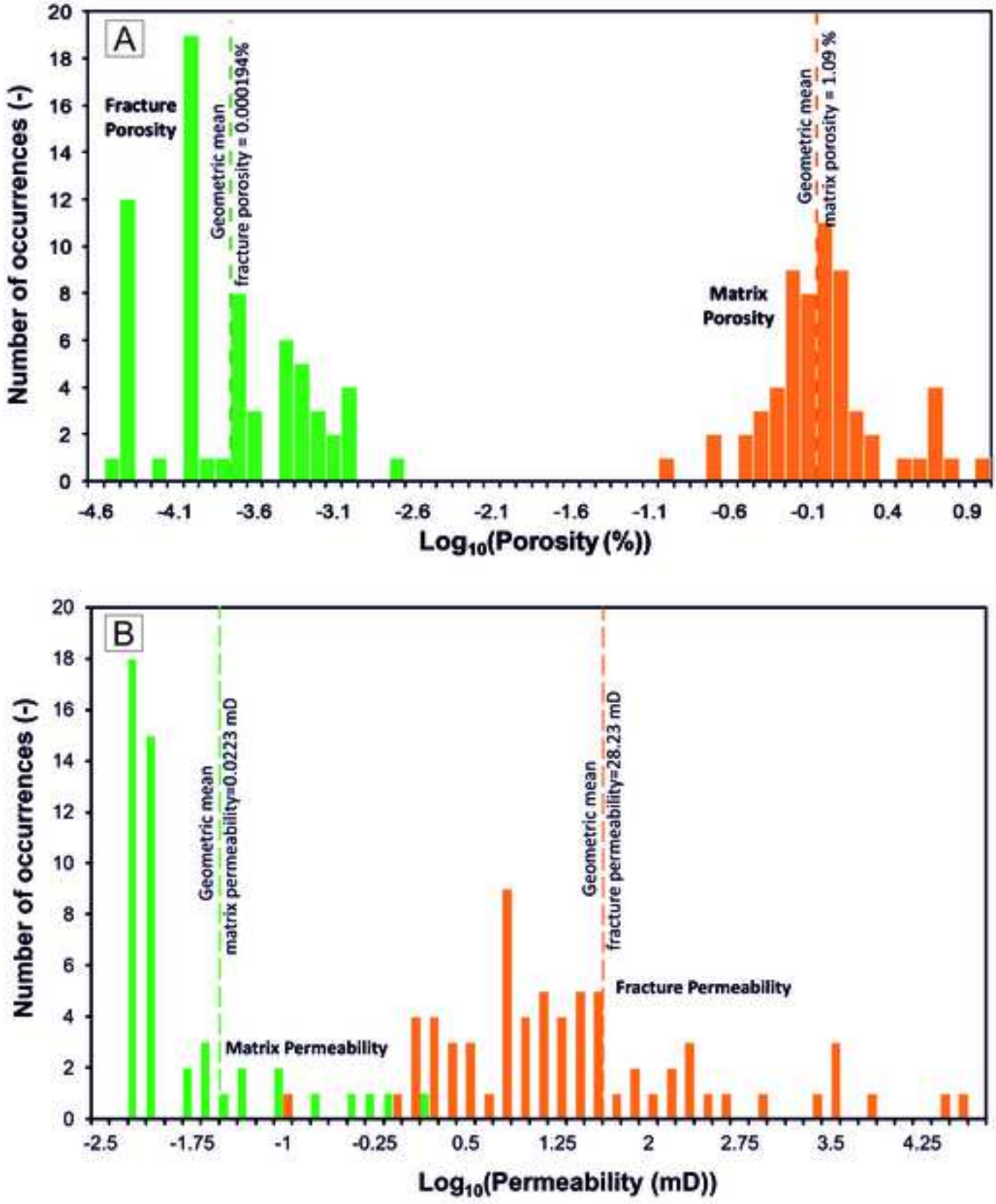

4.6 Permeability as a function of overburden pressure

The impact of confining pressure caused by overburden stress on fracture closure when the pore fluid pressure is reduced by production was examined. The permeability of a number of core plugs was measured, and sleeved core plugs were subjected to increasing hydrostatic pressures up to 4000 psi while the pore fluid pressure remained atmospheric due to the presence of a drainage path. Pore fluid pressures decrease during production, allowing the overburden stress to compact the rock by closing fractures as far as their asperities will allow. The degree of fracture closure depends on pressure differences and fracture orientation. An empirical equation for investigating the effects of stress on the magnitude of fracture permeability (Rashid, 2015) was applied in this study:

$$k(mD) = 0.74e^{(-0.0004P)} \quad (3)$$

where the pressure, *P*, is measured in psi. Cores with fracture permeabilities ranging across four orders of magnitude were selected to investigate permeability variations due to an increase in the confining pressure; permeabilities at zero stress were 5.2 mD, 50.7 mD, 389.3 mD and 4045.7 mD for the samples, respectively (Figure 13A-D). All four samples showed a reduction in permeability with increasing confining pressure. For each sample, the permeability fell to about 70% of its original magnitude once the maximum confining pressure (4000 psi) had been applied. Open natural macrofractures had fracture apertures greater than 0.10 mm, but despite losing nearly one-third of the original permeability, they still permitted fluid flow to occur because fracture apertures were not totally closed as a result of pressure changes during production.

5. DISCUSSION

Most fields in the Zagros fold-and-thrust belt and the eastern margin of the Arabian Plate produce hydrocarbons from fractured reservoir rocks. In these fields, unfractured matrix reservoirs are not considered to be sufficiently permeable to support commercial production (Mackertich and Samarrai, 2015; Rashid et al., 2015a; 2020).

Fractures in the Shiranish Formation are controlled by faulting and lithological variations (Jalili et al., 2020). Lithology is considered to be an essential control on fracturing in the Shiranish Formation, and closely spaced, discontinuous fractures with different lengths and apertures occur in harder, more cemented, indurated argillaceous limestones and brittle limestones (Wennberg et al., 2006; Dashti et al., 2018). However, faults and associated breccia zones have also enhanced the fracture frequency in different types of lithology in the formation.

Figure 13

Click here to access/download;Figure;Figure 13 .tif

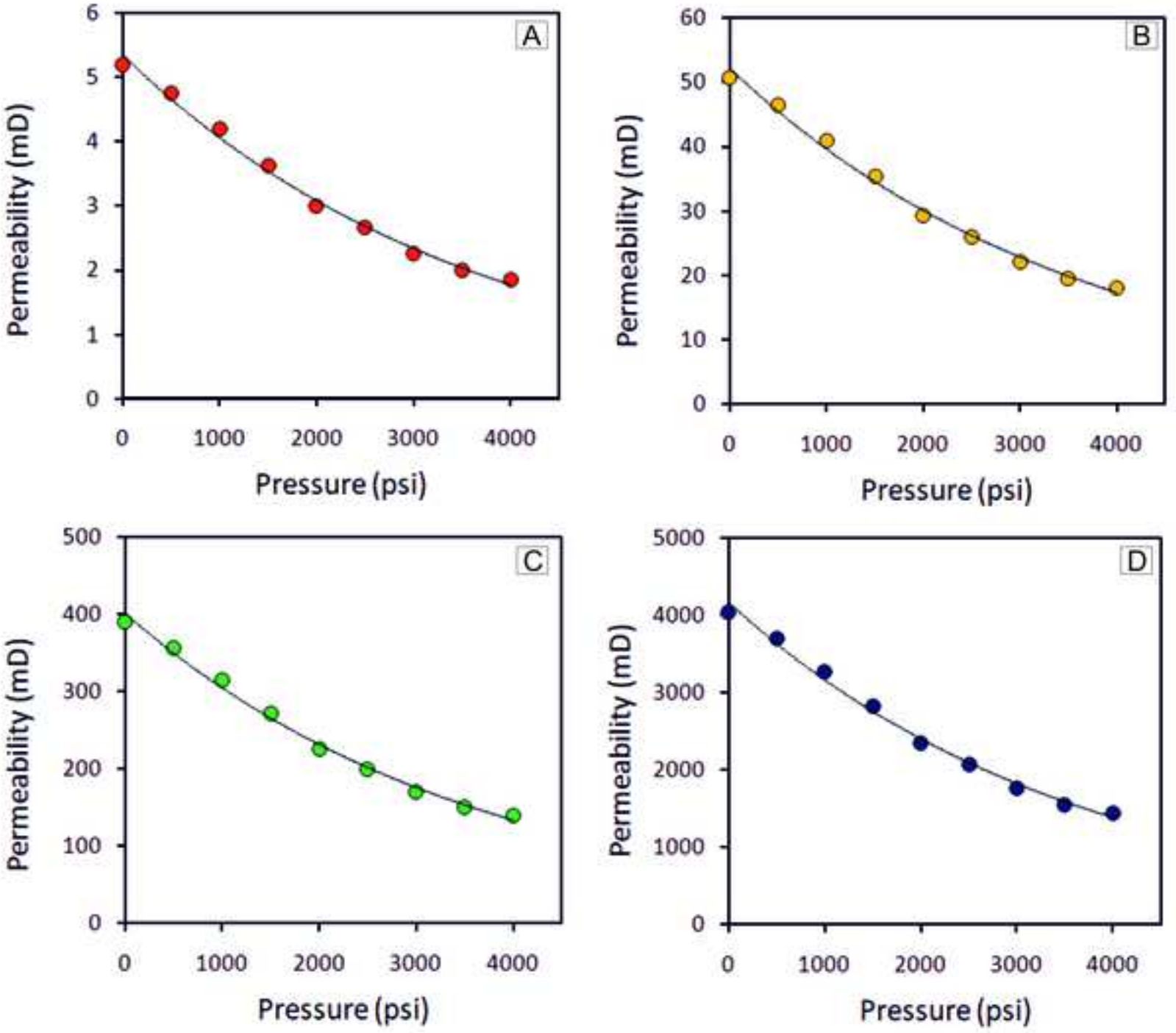

Fracture density increases close to fault zones. For example, in Well TT-05, about 50 clearly separate fractures were observed in a fault zone in only 5 m of core (fracture density = 10 fractures/m) (Figure 14). These fractures have a dominant strike parallel or oblique to the strike of the observed faults, and dip vertically to sub-vertically. These features demonstrate that the fractures have developed as a result of fault-derived stresses (Yale, 2003; Maerten et al., 2019; Rashid et al., 2020; Lao et al., 2020). By contrast, open and partially open fractures are oriented parallel to drilling/coring-related stress fields and to the regional present-day maximum horizontal compressive stress (σ_H) (Figure 10).

Vertical fracture frequency and horizontal spacing data, from the micro-resistivity image logs and the core samples, were analyzed to determine the relative vertical and horizontal distribution of fractures throughout the study intervals. The fracture frequency was obtained from the image logs as the number of fractures per meter of the logged interval. The measured data indicate a generally low fracture frequency for the Shiranish Formation, with 1.2 fractures/m in Well TT-05, 0.54 fractures/m in Well TT-06 and 0.36 fractures/m in Well TT-07 (Figure 14).

The fracture distribution throughout the drilled intervals was not homogeneous, but in general coincided with the presence of faults. The fracture distribution is illustrated by fracture density plots for the three wells, expressed as a 5 m moving average (Figure 14). The non-uniform distribution of fractures has influenced the magnitude of fracture porosity and permeability, and has resulted in a weak correlation between the calculated porosity and permeability for fractured intervals (Figure 15). Two different hydraulic flow units, HFU1 and HFU2, were identified based on the porosity-permeability trends from the fracture data set, with most of the fracture data corresponding to HFU1. Good correlations were observed from a power-law fit equation between porosity and permeability in HFU1 with a coefficient of determination $R^2 = 0.73$; correlations within the HFU2 samples were weaker ($R^2 = 0.49$). The goodness of fit of the relationship between porosity and permeability is probably related to the intense heterogeneity in the fracture properties as recorded at different scales.

The reservoir rocks of the studied intervals can be considered as “Type 2” reservoirs depending on fracture occurrence (*sensu* Nelson, 2001). In the absence of fractures, the matrix part of the Shiranish Formation can be classified as ‘non-reservoir’ or ‘tight’, and the very low matrix permeabilities are more typical of seal horizons within the Cretaceous succession. Fracturing has increased permeability values by up to four orders of magnitude according to the results from the core analyses, while fracture porosity is quite low and plays a negligible role in fluid storage. Furthermore, the low storage and flow capacity of the matrix is clearly apparent from the resistivity log profiles, as the LLS and LLD logs show very limited separations throughout the logged intervals

Figure 14

Click here to access/download;Figure;Figure 14.tif

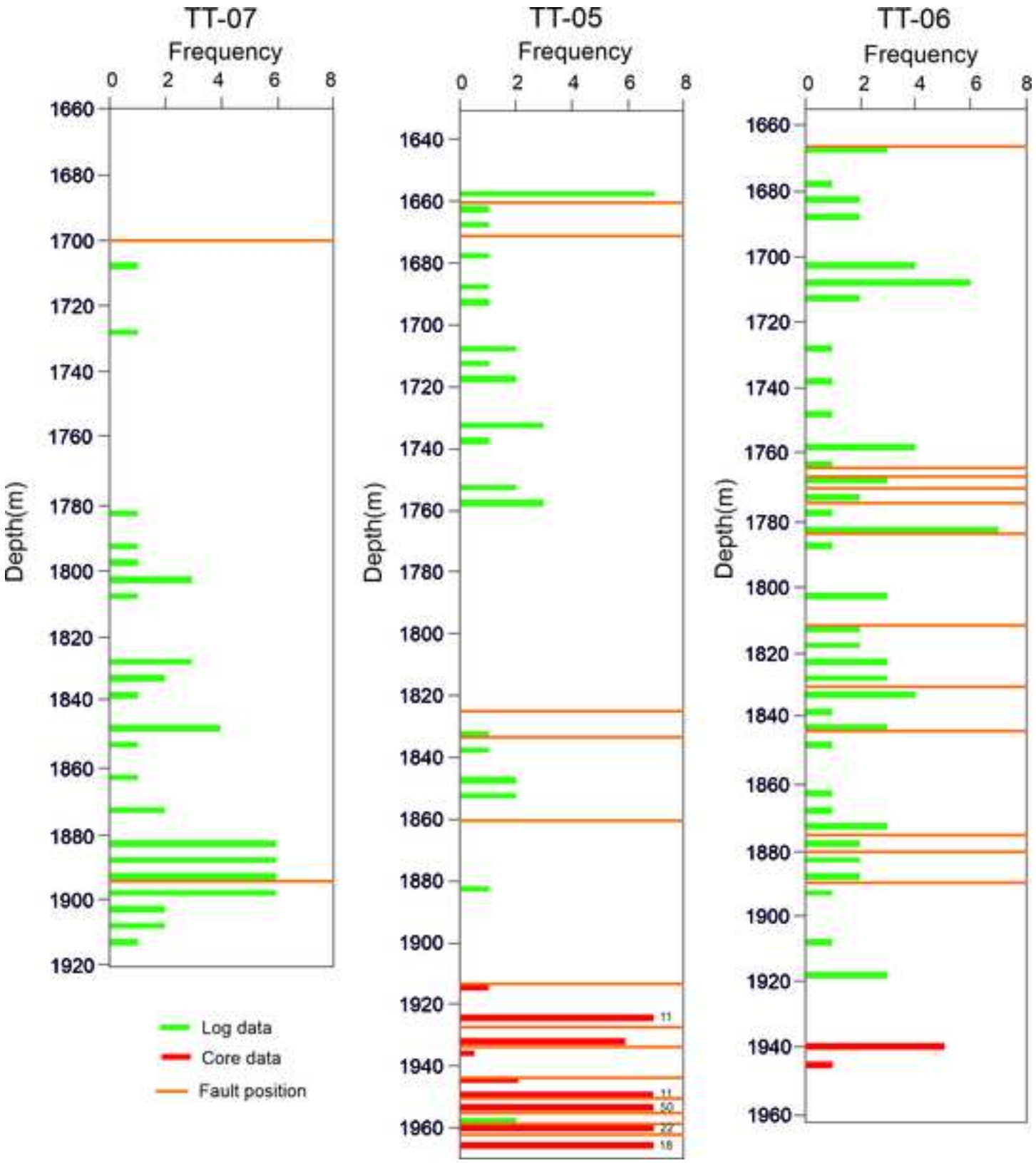

Figure 15

Click here to access/download;Figure;Figure 15 .tif

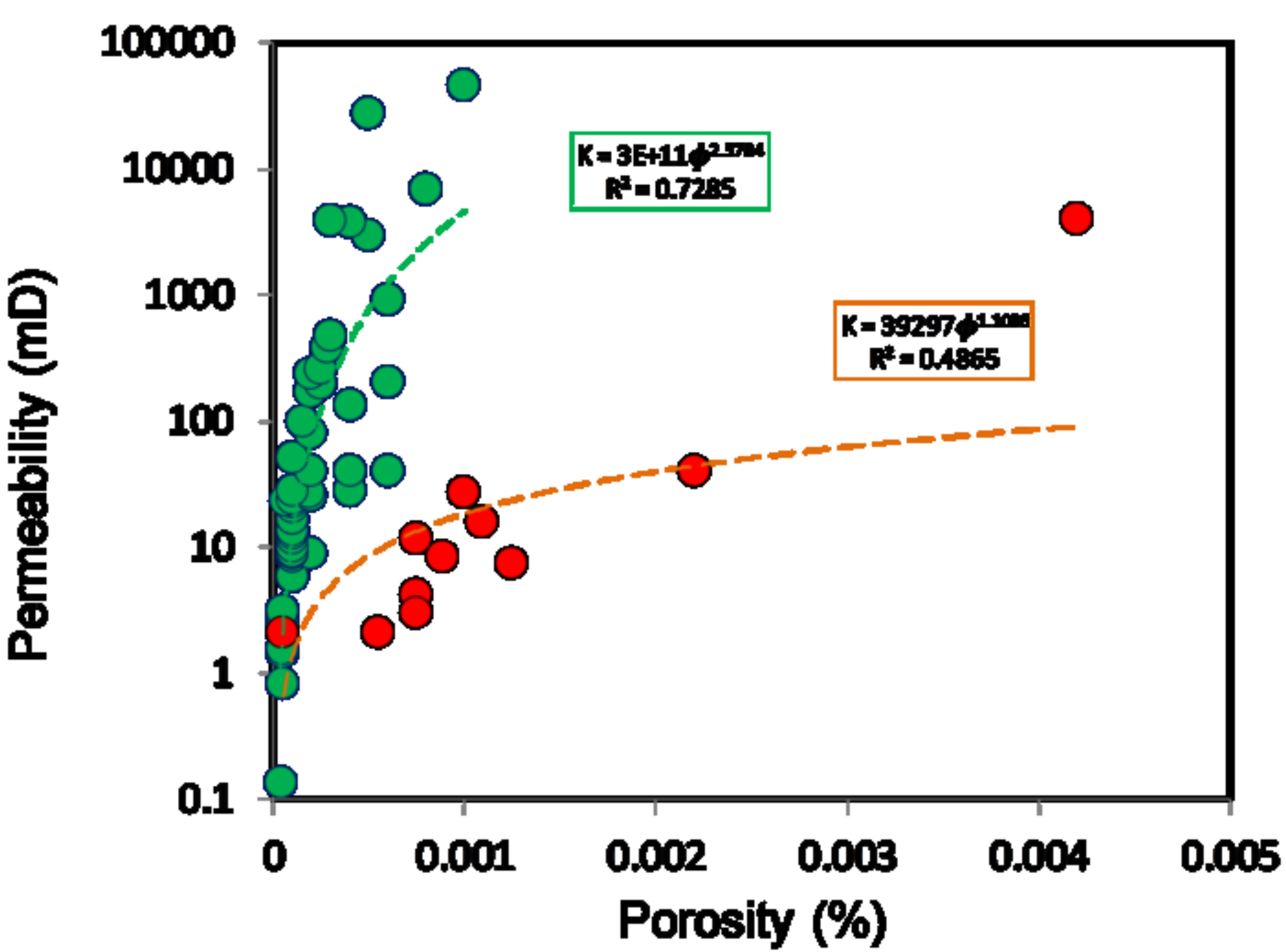

(Figure 7). The response of the resistivity logs to fluid distribution implies that the matrix permeability is very low and that interconnections between matrix pores fall below the 50 μm limit for mobile hydrocarbons according to the definition of potential porosity (Luo and Machel, 1995). In unfractured matrix, the pores are small and tight, capillary pressure considerations ensure that these pores contain predominantly water. When there are open fractures present, their larger apertures (larger than the pore sizes in the matrix) allow them to contain oil from the capillary pressure considerations, and that oil will be mobile if the fractures are connected.

By contrast, the flow rate data from the well tests indicate significant production from the fractured intervals. The Shiranish Formation locally contains abundant larger-scale conductive fractures that predominantly strike NE-SW and have average apertures of 0.17 mm, and which can be classified as macrofractures (Anders et al., 2014). Some of these macrofractures formed fluid flow conduits into the formation during drilling, since major mud losses occurred which resulted in the loss of cuttings returns and gas readings. These features may have been enhanced during drilling, but are likely to have been the main conduits for flow during well testing.

The magnitude of fracture permeability varies considerably with fracture attributes (Wu et al., 2020; Ferraro et al., 2020). However, depth profiles for natural fractures obtained from core samples (Figure 16) show that there are weak relationships between fracture frequency and apparent fracture permeability, especially in faults and fault damage zones.

Both the core and the image logs were checked where there seemed to be a correlation between enhanced permeability and fracture size parameters. In all cases evidence was found that fractures and fracture zones were the cause of the raised permeabilities. The zones for which this occurs are shown as grey boxes in Figure 16.

The maximum calculated fracture permeability (46,440 mD) was recorded at 1954.25 m in an interval, which has a fracture frequency of unity, while the highest fracture frequency (25) was recorded at 1956.95 m in an interval with a fracture permeability of 7.39 mD in Well TT-06. This result implies that fracture frequency does not necessarily control the magnitude of permeability and fluid flow, but other parameters such as fracture aperture and fracture height play a large role. Hence, the fracture frequency parameter has a limited influence on the permeability distribution in fractured carbonate intervals in the studied reservoir. This could be related to the occlusion of fracture spaces by authigenic cements and the weak connectivity of fractures close to fault damage zones (Evans et al., 1997; Billi et al., 2003; Micarelli et al., 2006; Haines et al., 2016).

It was mentioned in the methodology that permeabilities can be erroneous when estimated using a cubic law. This is because the Hagen-Poiseuille cubic law assumes the fracture is of infinite extent with a uniform aperture and smooth fracture surfaces, none of which is the case for real fractures

Figure 16

Click here to access/download;Figure;Figure16 .tif

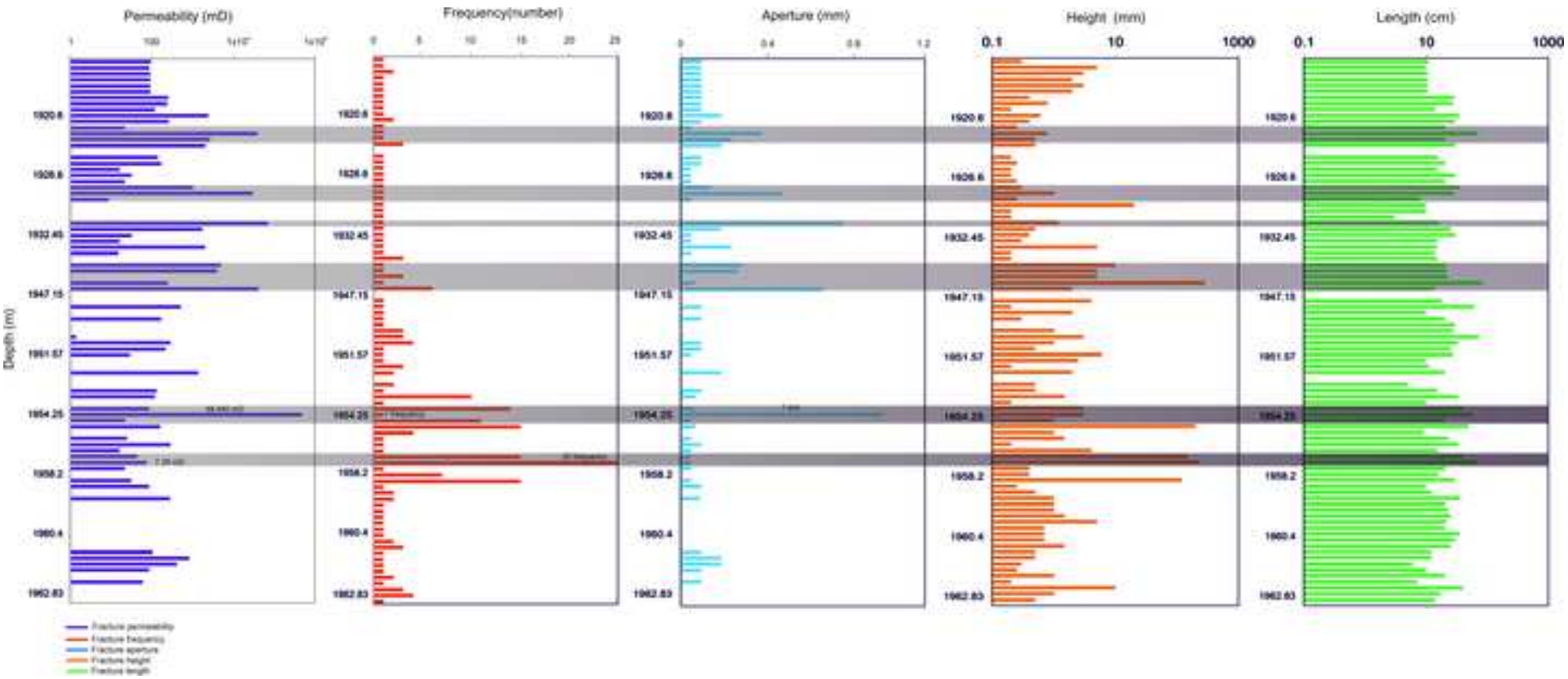

(Glover and Hayashi, 1997). The usual consequence is that the actual permeability is less than that predicted with the cubic law. This can be taken account of by using an hydraulic aperture in Equation (2) in place of a physical aperture.

The cross-plot in Figure 17a demonstrates that there is a power-law relationship between fracture aperture and calculated fractured permeability. In this figure, permeability in millidarcies is plotted as a function of fracture aperture (in mm) and is shown with the best fit curve with a forced cubic exponent (R^2=0.9884) and the upper and lower envelopes. Fractures with apertures equal to or greater than 0.10 mm improved the permeability of the Shiranish Formation. The maximum calculated individual fracture permeability (46,440 mD) coincides with the largest fracture aperture (1.0 mm), and the minimum calculated individual fracture permeability (0.14 mD) arose from the smallest fracture aperture (0.013 mm).

It should be noted that the fit in Figure 17a is a cubic law fit on aperture, which is consistent with the Hagen-Poiseuille law for planar fluid flow between two smooth plates, and is stated in Equation (2) above. The deviations of individual points in Figure 17 from the general behaviour can be ascribed to the operation of different degrees of surface roughness for different fractures, and hence different values of A_h/A_m. If we can assume fluid to flow in the fractures as if they had smooth planar face, we can use the fit to the experimental to calculate the mean length of the fractures crossing the borehole, as follows. Figure 17b contains the same data and fits as in Figure 17a, but plotted on double-logarithmic axes where permeability is shown as a function of the aperture cubed (A^3). This figure also converts the units of permeability to m^2 and of aperture cubes to m^3. The linear trend exhibited by the data values over 6 orders of magnitudes shows how well the data fits a cubic model. The coefficients from the theoretical lines are 0.03949 m^{-1}, 0.01234 m^{-1} and 0.1184 m^{-1} for the best fit, lower bound and upper bound respectively. According to Equation (2) these values are equal to $1/12L$, where L is the mean length of fractures in the formation, providing the 18 data points are representative. Consequently, we can calculate a mean length of fractures to be 2.11 m, with a lower bound of 0.7036 m and an upper bound of 6.755 m.

It should be noted that in general fluid flow in a fracture is also affected by the roughness of a fracture surface, which has been modelled (Glover et al., 1997; 1998a; Ogilvie et al., 2003; 2006; et al., 2006) and tested in the field (Glover et al., 1998b). In this case the flow in a fracture is always lower than that predicted by the Hagen-Poiseuille planar model, implying that either the aperture is greater in reality, or in our case, where the aperture is measured independently, the calculated fracture length is smaller than those calculated above. Glover et al. (1998b) found that the ratio of the hydraulic aperture to mean aperture was 0.72 for a single fracture for the Hachimantai geothermal site in Japan. In other words, the effective aperture for fluid flow is 0.72 of the mechanical aperture. In other words

Figure 17

Click here to access/download;Figure;Figure 17 .tif

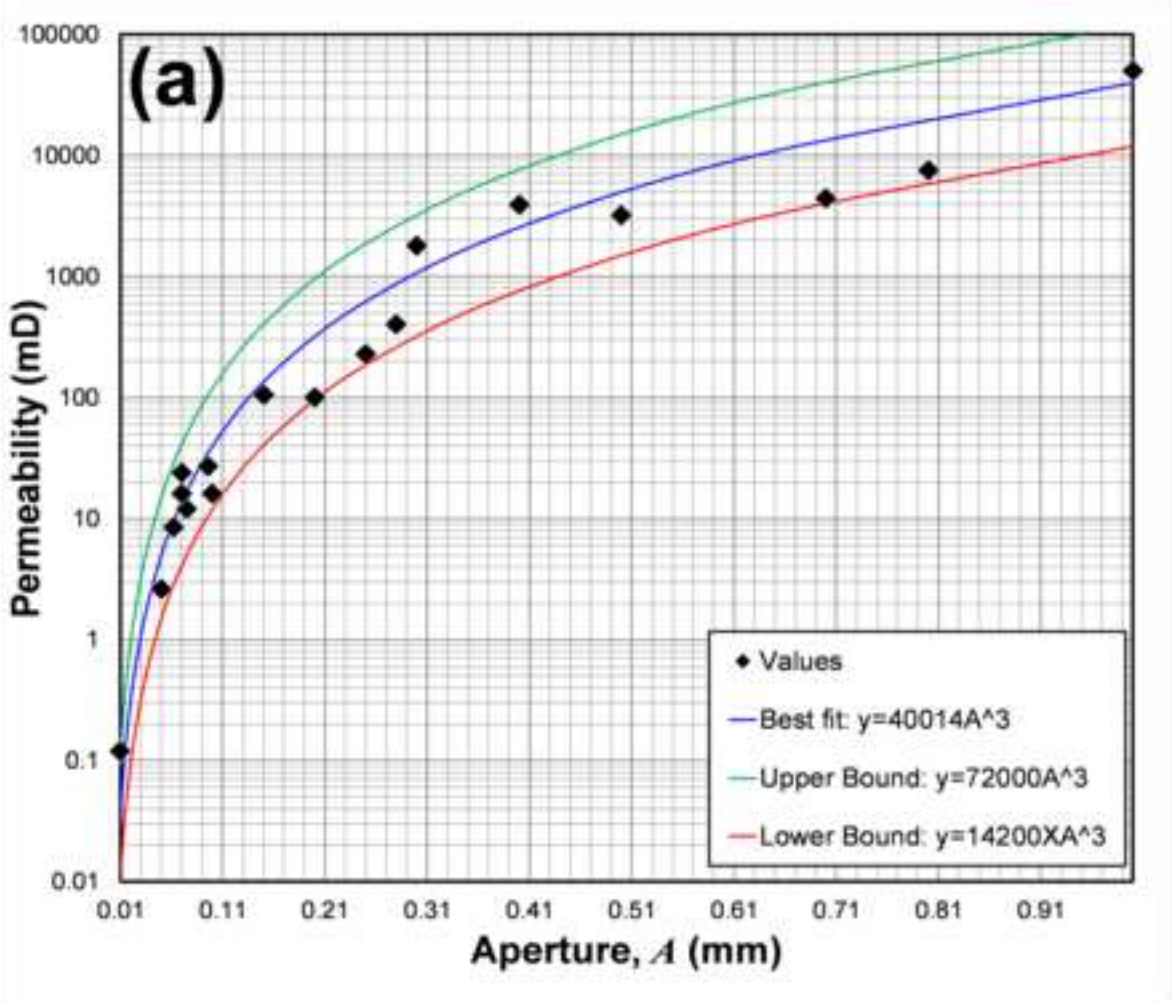

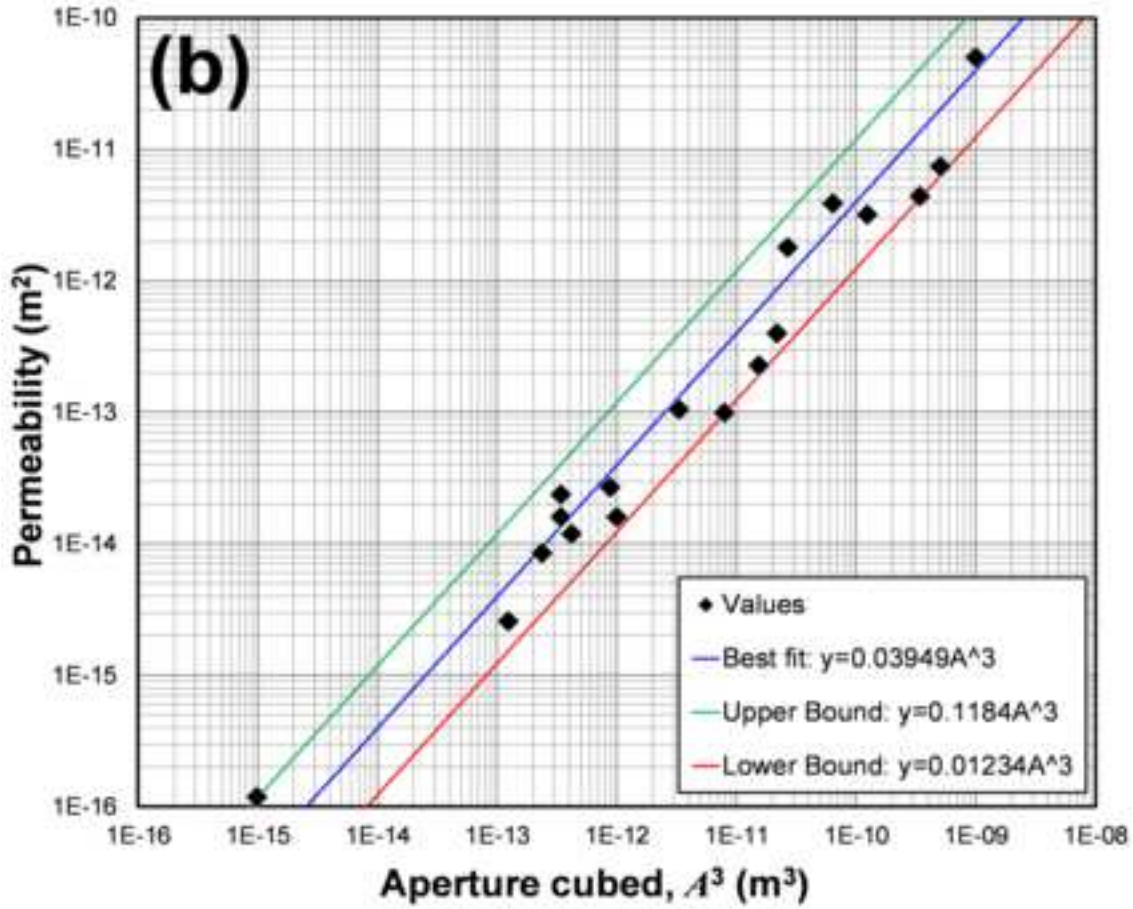

not accounting for rough fracture surfaces results in an overestimation of permeability by a factor of about 1.39 (i.e., 39%).

While the Glover et al. (1998b) data is for a volcanic tuff rather than carbonate, it is an indication that the magnitude of the size of the perturbation caused by fracture roughness is approximately a reduction of the aperture by about 28%. Figure 18 shows a model of the Hachimantai fracture data using Synfrac©, showing the degree of roughness and long wavelength matching that leads to a hydraulic to mean aperture of 0.72. If this is applied to the calculations on the data from Figure17b, the calculated fracture lengths increase to 5.65 m, 1.88 m and 18.09 m, for the mean fracture length, the lower bound and the upper bound, respectively.

In addition to fracture aperture, fracture height also has an impact on the magnitude of fracture permeability. This parameter, in combination with the fracture surface, describes a corridor for fluid flow in reservoir rocks that have negligible matrix porosity and permeability. Furthermore, the fracture length remains as a dependable element for the magnitude of fracture permeability. The fracture lengths from the core samples recorded homogeneous distributions (Figure 16), while the magnitude of the fracture permeability was found to be heterogeneous and was not influenced by fracture length.

The open, drilling-induced fractures were formed parallel to the regional present-day maximum horizontal compressive stress (σ_H) (Lai et al., 2018; Zhang et al., 2018; Shen et al., 2018; Pham et al., 2020). In the Taq Taq field, these types of fractures strike NE-SW (Figure 10). Open fractures in tight carbonates at the Taq Taq structure also have a NE-SW strike, parallel to σ_H and perpendicular to the axis of the anticline (Figure 10). These fracture apertures remain as effective openings (Lai et al., 2017; Rashid et al., 2020b), and provide interconnected pathways for fluid movement through the reservoir. In addition, authigenic cement fills may help to preserve open fractures, as the cements may prevent the aperture from closing and collapsing (Rashid et al., 2020b). This type of fracture may remain open and conductive for fluid flow.

The population of NE-SW striking fractures can be observed at different structures in the Zagros fold-and-thrust belt including the Safin and Banabawi structures in the Low Folded Zone, and Miran West structure in the High Folded Zone (Reif et al., 2012; Rashid et al., 2020). These fractures are considered to be the dominant producing type in discovered fields. NE-SW trending fractures are likely to be open within the present day maximum horizontal stress throughout the NE part of the Arabian Plate (oriented N45W), as we have observed in the Taq Taq field.

Production data on tight carbonates in the Shiranish Formation are consistent with fracture distribution and frequency. Flow rate tests showed that commercial oil flows occur from wells in which there is a dominant set of open and partially-open fractures parallel to the fold axis. The results of the

Figure 18

Click here to access/download;Figure;Figure 18.JPG

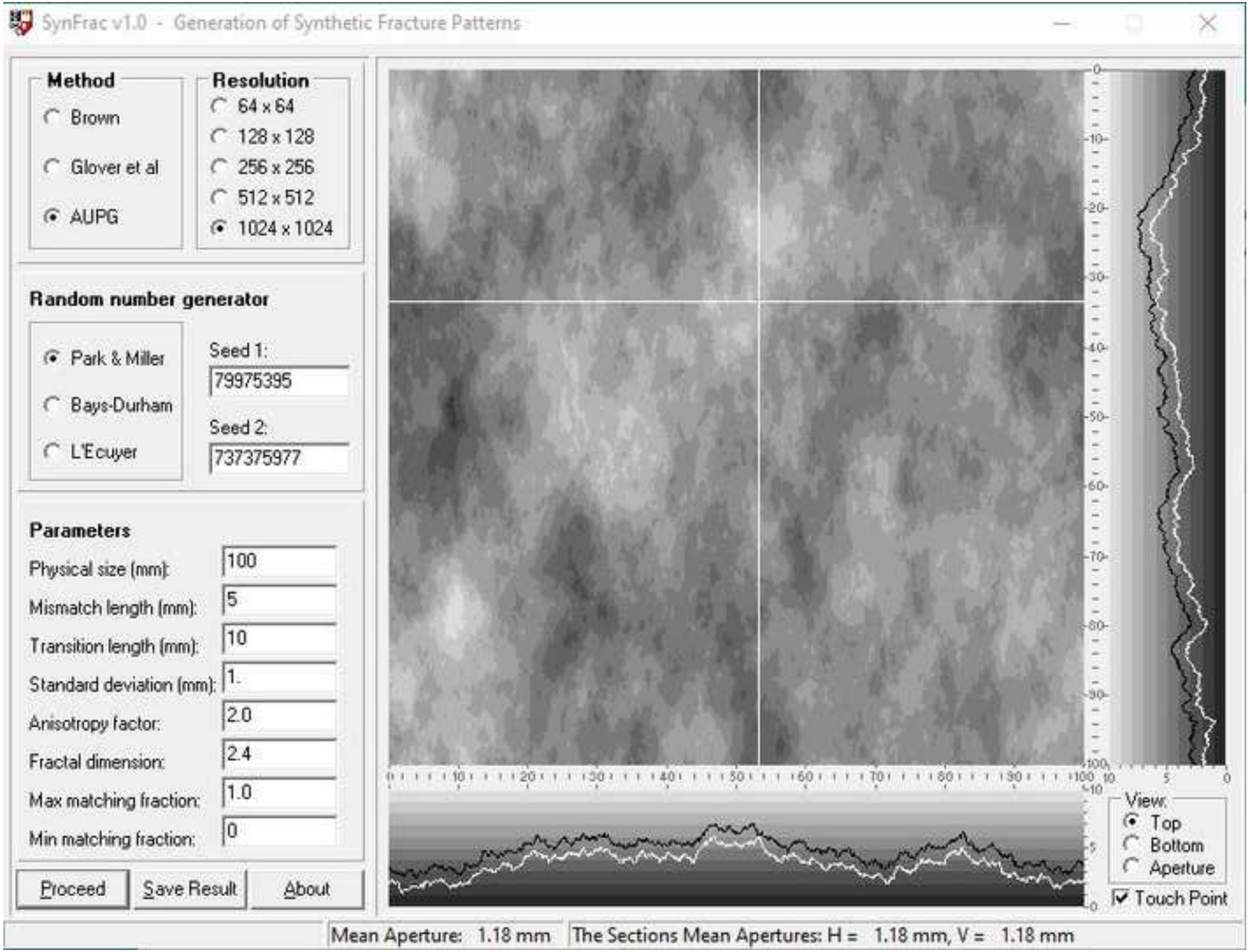

present study show that these types of fractures potentially form interconnected macrofractures. In Well TT-06, the oil production rate is higher than that in wells TT-05 and TT-07. This is probably due to the increased fracture density and fracture continuity (vertical and lateral extent), which have resulted in the formation of high permeability pathways and super-permeability zones (Rotevatn and Bastesen, 2012; Yue et al., 2018; Bagni et al., 2020; Li et al., 2020). Furthermore, extensive mud losses that were recorded at 1810 m and 1938 m may be linked to fracture occurrence and high permeability zones. The fractures in Well TT-06 extend almost continuously from the top to the bottom of the Shiranish Formation (Figure 14). In contrast, the fracture distribution was confined to the central part of the formation in Well TT-05 and the upper part in Well TT-07. The lower fluid movement and productivity may have been influenced by other parameters such as occluded fractures, especially in cemented breccia zones.

6. CONCLUSIONS

This study analyzed fracture systems in tight reservoir carbonates in the Shiranish Formation in the Taq Taq field in northern Iraq. The contribution of fractures to reservoir permeability and fluid flow was investigated using cores, wireline logs, well tests and mud log data, and represents the most comprehensive study of this type. The novelty of the work is that it represents an integrated core and wireline petrophysical, geomechanical, fracture and geological study of a typical middle eastern carbonate reservoir. Individual major findings are given in the following paragraphs.

The magnitude of reservoir porosity comprising matrix and fracture porosity is very low, especially where fracture volumes are considered to be negligible. The Shiranish Formation reservoir should therefore be modelled as a tight carbonate in terms of its matrix storage capacity. Reservoir productivity is dominated by fractures, and the magnitude of fracture permeability is four orders of magnitude greater than the magnitude of matrix permeability. Natural open and partially-open macrofractures control the provision of interconnected fracture networks and the creation of fluid flow pathways for hydrocarbon migration. Consequently, fracture characterisation and distribution need to be considered during early field optimization planning in newly-discovered fields in the Zagros fold-and-thrust belt in order to prevent early water breakthrough.

The structural analysis implied that the dominant fractures controlling fluid flow and hydrocarbon production within the studied intervals, consisting of open and partially-open natural fractures, have an average fracture aperture greater than 0.10 mm (macrofractures). These types of fractures have sub-vertical to vertical dip angles and a dominant NE-SW strike which is parallel to the strike of the observed faults and perpendicular to the axis of the Taq Taq structure.

Analysis of the fracture frequency showed that there was a heterogeneous distribution of fractures in the wells studied. The fracture frequency is dominantly controlled by lithological variations and the positions of faults, and a higher number of fractures was observed in harder rocks and in fracture zones related to fault cores. The fracture frequency influences the fracture permeability distribution but does not have the same impact on the magnitude of fracture permeability. By contrast, fracture permeability is dominantly controlled by the fracture aperture scale, as the highest permeability was linked to the largest fracture aperture.

Calculations based on the Hagen-Poiseuille law of the permeability data as a function of aperture indicate that the mean length of the fractures is 2.11 m if the fractures are smooth, or more likely up to 5.65 m if they have rough surfaces, and fall between the values of 0.704 m and 6.755 m, if smooth, and between 1.88 m and 18.09 m, if rough.

The fracture orientations coincide with the trend of the regional present-day maximum horizontal compressive stress (σ_H) in the Zagros fold-and thrust belt as evidenced by data from the World Stress Map (Heidbach et al., 2016). The similarity between both the dip and strike of the induced fractures with both core and wireline-derived dips and strikes of existing fractures and faults as well as the world stress map data indicates that all the data is not only self-consistent but that the stress regime in the region has not changed appreciably since fracturing was active (i.e., within the last 25 Ma). The directional data in this study seems to be consistent with values of the direction of maximum principal horizontal stress from the world stress map data for reservoirs in all of Iraq and Iran, and probably for most of Saudi Arabia.

The open and partially-open fracture apertures were not influenced by the maximum horizontal stress, and fracture surfaces remain open. The fracture-filling minerals in partially-open fractures acted to prevent the closure of the fracture surfaces and the occlusion of the fracture aperture as a result of external stress. Furthermore, the confining pressure derived from fluid production during field development reduced the original permeability by nearly one-third in different fracture apertures in open fractures. However, fractures with apertures greater than 0.10 mm remain productive at 4000 psi confining pressure, while smaller fractures were closed and would play no role in fluid production.

ACKNOWLEDGEMENTS

The authors would like to express their appreciation to Genel Energy - Sulaimani Office and the geology team for providing well reports and the raw data for this research.

Data availability statement

A summary of fracture data is available at https://zenodo.org/record/7756301. The Synfrac© software can be obtained at https://zenodo.org/record/7756282.

REFERENCES

ABDULLAH, H. G., COLLIER, R. E. L. and MOUNTNEY, N. P. , 2019. The palaeoshoreline of Early Miocene formations (Euphrates and Jeribe) at the periphery of the Zagros Foreland Basin, Sulaimani Governorate, Kurdistan Region, NE Iraq. Arabian Journal of Geosciences, 12, 547.

AFŞAR, F., WESTPHAL, H. and PHILIPP, S.L., 2014. How facies and diagenesis affect fracturing of limestone beds and reservoir permeability in limestone–marl alternations. Marine and Petroleum Geology, 57, 418-432.

AL-KHALIFAH, H., GLOVER, P.W.J. and LORINCZI, P., 2020. Permeability prediction and diagenesis in tight carbonates using machine learning techniques. Marine and Petroleum Geology, 112, 109096.

ALLSHORN, S.A., DAWE, R.A. and GRATTONI, C.A., 2019. Implication of heterogeneities on core porosity measurements. Journal of Petroleum Science and Engineering, 174, 486-494.

AL SHDIDI, S., THOMAS, G., DELFAUD, J., 1995. Sedimentology, Diagenesis, and Oil Habitat of Lower Cretaceous Qamchuqa Group, Northern Iraq. AAPG Bulletin, 79 (5), 763-778.

AL-QAYIM, B. and RASHID, F., 2012. Reservoir Characteristics of The Albian Upper Qamchuqa Formation Carbonates, Taq Taq Oilfield, Kurdistan, Iraq. Journal of Petroleum Geology, 35, 317-341.

ANDERS, M.H., LAUBACH, S.H. and SCHOLZ, C.H., 2014. Microfractures: A review. Journal of Structural Geology, 69, part B , 377-394.

AQRAWI, A. A. M., GOFF, J. C., HORBURY, A. D. and SADOONI, F. N., 2010. The Petroleum Geology of Iraq. Scientific Press, Beaconsfield, UK, 424 pp.

BAGNI, F.L., BEZERRA, F.H., BALSAMO, F., MAIA, R.P. and DALL'AGLIO, M., 2020. Karst dissolution along fracture corridors in an anticline hinge, Jandaíra Formation, Brazil: Implications for reservoir quality. Marine and Petroleum Geology, 115, 104249.

BAGRINTSEVA, K.I., 2015. Carbonate Reservoir Rocks, John Wiley & Sons INC International Concepts, 352 pp., ISBN:9781119083573

BILLI, A., SALVINI, F. and STORTI, F., 2003.The damage zone-fault core transition in carbonate rocks: implications for fault growth, structure and permeability. Journal of Structural Geology, 25, 11, 1779-1794.

BUDAY, T., 1980. The Regional Geology of Iraq. In: Stratigraphy and Palaergeography, vol. 1. Publications of GEOSURV, Baghdad, p. 445.

CHU, D., GORDON, R.G., 1998. Current plate motions across the Red Sea, *Geophysical Journal International*, 135(2), 313–328, https://doi.org/10.1046/j.1365-246X.1998.00658.x

DASHTI, R. RAHIMPOUR-BONAB, H. and ZEINALI, M., 2018. Fracture and mechanical stratigraphy in naturally fractured carbonate reservoirs-A case study from Zagros region. Marine and Petroleum Geology, 97, 466-479.

DERSHOWITZ, W.S. and HERDA, H.H., 1992. Interpretation of fracture spacing and intensity, Proceedings of the 33rd U.S. Symposium on Rock Mechanics, eds. J. R. Tillerson, and W. R. Wawersik, Rotterdam, Balkema, p. 757-766.

DICKSON, J. A. D. 1965. A Modified Staining Technique for Carbonates in Thin Section. Nature, 205, 587-587.

DICKSON, J. A. D. 1966. Carbonate identification and genesis as revealed by staining Sedimentary petrology, 36, 492-505.

DONALDSON, E.C. and TIAB, D., 2004. Theory and Practice of Measuring Reservoir Rock and Fluid Transport Properties. Gulf Professional Publishing, Elsevier.

DUNHAM, R. J. 1962. Classification of carbonate rocks according to depositional texture. In: Ham, W.E., ed., Classification of Carbonate rocks: AAPG-Publ-Memoris 1, Tulsa, Oklahoma., 108-121.

ENGLISH, J.M., LUNN, G.A., FERREIRA, L. and YACU, G., 2015. Geologic evolution of the Iraqi Zagros, and its influence on the distribution of hydrocarbons in the Kurdistan region. AAPG Bulletin, 99, 2, 231-272.

EVANS, J.P., FORSTER, C.B. and GODDARD, J.V., 1997. Permeability of fault-related rocks, and implications for hydraulic structure of fault zones. Journal of Structural Geology, 19, 11, 1393-1404.

EZATI, M., AZIZZADEH, M., RIAHI, M.A., FATTAHPOUR, V. and HONARMAND, J., 2018. Characterization of micro-fractures in carbonate Sarvak reservoir, using petrophysical and geological data, SW Iran. Journal of Petroleum Science and Engineering, 170, 675-695.

FERRARO, F., AGOSTA, F., PRASAD, M., VINCIGUERRA, S., VIOLAY, M. and GIORGIONI, M., 2020. Pore space properties in carbonate fault rocks of peninsular Italy. Journal of Structural Geology, 130, 103913.

FLÜGEL, E., 2004. Microfacies Analysis of Limestones: Analysis, Interpretation and Application. Springer Verlag, Berlin, pp. 976.

FU, Q., HU, S., XU, Z., ZHAO, W., SHI, S. and ZENG, H., 2020. Depositional and diagenetic controls on deeply buried Cambrian carbonate reservoirs: Longwangmiao Formation in the Moxi–Gaoshiti area, Sichuan Basin, southwestern China. Marine and Petroleum Geology, 117, 104318.

GARLAND, C. R., ABALIOGLU, I., AKCA, L., CASSIDY, A., CHIFFOLEAU, Y., GODAIL, L., GRACE, M. A. S., KADER, H. J., KHALEK, F., LEGARRE, H., NAZHAT, H. B. and SALLIER, B., 2010. Appraisal and development of the Taq Taq field, Kurdistan region, Iraq. Geological Society, London, Petroleum Geology Conference Series, 7, 801-810.

GARLAND, J., NEILSON, J., LAUBACH, S. E. and WHIDDEN, K. J., 2012. Advances in carbonate exploration and reservoir analysis. Geological Society, London, Special Publications, 370, 1-15.

GHAFUR, A. A., 2020. The origin, differential diagenesis and microporosity characteristics of carbonate mud across a late Paleogene ramp (Iraqi Kurdistan region). Journal of Petroleum Science and Engineering, 192, 107247.

GHAFUR, A.A., HERSI, O.S., SISSAKIAN, V.K., KARIM, S., ABDULHAQ, H.A. and OMER, H.O., 2020. Sedimentologic and stratigraphic properties of Early Cretaceous Neo-Tethys shelf margin of Arabia: The Qamchuqa Formation of the Zagros Folded zone – Kurdistan Region of Iraq. Marine and Petroleum Geology, 118, 104421.

GLOVER, P.W.J. and BORMANN, P., 2007. The characterization of trough and planar cross-bedding from borehole image logs. Journal of Applied Geophysics, 62(2), 178-191.

GLOVER, P.W.J., MATSUKI, K., HIKIMA, R. and HAYASHI, K., 1998a. Synthetic rough fractures in rocks. Journal of Geophysical Research: Solid Earth, 103(5), pp. 9609-9620.

GLOVER, P.W.J., MATSUKI, K., HIKIMA, R. and HAYASHI, K., 1998b. Fluid flow in synthetic rough fractures and application to the Hachimantai geothermal hot dry rock test site. Journal of Geophysical Research: Solid Earth, 103(5), pp. 9621-9635.

GLOVER, P.W.J. and HAYASHI, K., 1997. Modelling fluid flow in rough fractures: Application to the Hachimantai geothermal HDR test site. Physics and Chemistry of the Earth, 22(1-2 SPEC. ISS.), pp. 5-11.

GLOVER, P.W.J., MATSUKI, K., HIKIMA, R. and HAYASHI, K., 1997. Fluid flow in fractally rough synthetic fractures. Geophysical Research Letters, 24(14), pp. 1803-1806.

HAINES, T.J., MICHIE, E.A.H., NEILSON, J.E. and HEALY, D., 2016. Permeability evolution across carbonate hosted normal fault zones. Marine and Petroleum Geology, 72, 62-82.

HEIDBACH, O., M. RAJABI, X. CUI, K. FUCHS, B. MÜLLER, J. REINECKER, K. REITER, M. TINGAY, F. WENZEL, F. XIE, M. O. ZIEGLER, M.-L. ZOBACK, and M. D. ZOBACK., 2018. The World Stress Map

database release 2016: Crustal stress pattern across scales. Tectonophysics, 744, 484-498. http://doi.org/10.1016/j.tecto.2018.07.007

HUSSEIN, D. COLLIER, R. LAWRENCE. J. RASHID, F. GLOVER, P.W.J., LORINCZI, P. and BABAN, D.H., 2017. Stratigraphic correlation and paleoenvironmental analysis of the hydrocarbon-bearing Early Miocene Euphrates and Jeribe formations in the Zagros folded thrust-belt. Arabian Journal of Geosciences, 10, pp. 543-554.

HUSSEIN, D., LAWRENCE, J., RASHID, F., GLOVER, P. and LORINCZI, P., 2018. Developing pore size distribution models in heterogeneous carbonates using especially nuclear magnetic resonance. In Engineering in Chalk: Proceedings of the Chalk 2018 Conference, pp. 529-534. ICE Publishing. Hydrogeol. J. 24, 1147–1170.

JALILI, Y., YASSAGHI, A., KHATIB, M.M. and GOLALZADEH, A., 2020. Effect of transverse faults on fracture characteristics and borehole instability in the Asmari reservoir of Zagros folded belt zone, Iran. Journal of Petroleum Science and Engineering, 188, 106820.

JASSIM, S.Z. and GOFF, J.C., 2006. The Geology of Iraq. Dolin, Prague, 341 pp.

KOSARI, E., KADKHODAIE, A., BAHROUDI, A., CHEHRAZI, A. and TALEBIAN, M., 2017. An integrated approach to study the impact of fractures distribution on the Ilam-Sarvak carbonate reservoirs: A case study from the Strait of Hormuz, the Persian Gulf. Journal of Petroleum Science and Engineering, 152, 104-115.

KULANDER, B.R., DEAN, S.L. and WARD, B.J., 1990. Fractured core analysis: interpretation, logging, and use of natural and induced fractures in core (Vol. 8). Tulsa: American Association of Petroleum Geologists.

LAI, J., WANG, G., WANG, S., CAO, J., LI, M., PANG, X., HAN, C., FAN, X., YANG, L., HE, Z., QIN, Z., 2018. A review on the applications of image logs in structural analysis and sedimentary characterization. Marine and Petroleum Geology, 95, 139–166.

LAI, J., WANG, G., FAN, Z., CHEN, J., WANG, S. and FAN, X., 2017. Sedimentary characterization of a braided delta using well logs: the upper Triassic Xujiahe Formation in Central Sichuan basin, China. J. Petrol. Sci. Eng. 154, 172–193.

LAO, H., SHAN, Y., WANG, Y. and WU, Z., 2020. Characteristics of growth fault architecture and its evolution in mudstone strata: Evidence from the core of Bohai Bay basin. Marine and Petroleum Geology, 119, 104503.

LAW, D., MUNN, A., SYMMS, D., WILSON, S., HATTINGH, R., BOBLECKI, K., AL MAREI, P., CHERNIK, D. PARRY and HO, J., 2014. Competent person's report on certain petroleum interests of Gulf Keystone Petroleum and its subsidiaries in Kurdistan, Iraq. ERC Equipoise Ltd, 114.

LUO, P., MACHEL, G., 1995. Pore size and pore throat types in a heterogeneous dolostone reservoir; Devonian Grosmon Formation, Western Canada basin. Am. Assoc. Petrol.Geol. Bull. 79, 1698–1720.

LI, C., ZHAO, L., LIU, B., LIU, H., LI, J., FAN, Z., WANG, J., LI, W., ZHAO, W. and SUN, M., 2020. Origin, distribution and implications on production of bedding-parallel fractures: A case from the Carboniferous KT-Formation in the NT oilfield, Precaspian Basin, Kazakhstan. Journal of Petroleum Science and Engineering, in press, 107655.

MACKERTICH, D.S. and SAMARRAI, A.I., 2015. History of hydrocarbon exploration in the Kurdistan Region of Iraq. GeoArabia, 20(2), pp. 181-220.

MAERTEN, L., LEGRAND, X., CASTAGNAC, C., LEFRANC, M., JOONNEKINDT, J. and MAERTEN, F., 2019. Fault-related fracture modeling in the complex tectonic environment of the Malay Basin, offshore Malaysia: An integrated 4D geomechanical approach. Marine and Petroleum Geology, 105, 222-237.

MATSUKI, K., CHIDA, Y., SAKAGUCHI, K. and GLOVER, P.W.J., 2006. Size effect on aperture and permeability of a fracture as estimated in large synthetic fractures. International Journal of Rock Mechanics and Mining Sciences, 43(5), pp. 726-755.

MENEZES, D.F., BEZERRA, F.H., BALSAMO, F., ARCARI, A., MAIA, R.P. and CAZARIN, C.L., 2020. Subsidence rings and fracture pattern around dolines in carbonate platforms – Implications for evolution and petrophysical properties of collapse structures. Marine and Petroleum Geology, 113, 104113.

MICARELLI, L., BENEDICTO, A. and WIBBERLEY, C.A.J., 2006. Structural evolution and permeability of normal fault zones in highly porous carbonate rocks. Journal of Structural Geology, 28, 7, 1214-1227.

MICHAEL, A. and GUPTA, I., 2020. Analytical orientation criteria for drilling and completion-induced fracture initiation considering fluid infiltration from the wellbore. Journal of Petroleum Science and Engineering, 190, 107033.

MICHIE, E.A.H., 2015. Influence of host lithofacies on fault rock variation in carbonate fault zones: a case study from the Island of Malta. Journal of Structural Geology, 76, 61–79.

MOHAMMED SAJED, O.K. and GLOVER, P.W.J., 2020. Dolomitisation, cementation and reservoir quality in three Jurassic and Cretaceous carbonate reservoirs in north-western Iraq. Marine and Petroleum Geology, 115.

MOHAMMED SAJED, O.K., GLOVER, P.W.J. and COLLIER, R.E.L., 2021. Reservoir quality estimation using a new ternary diagram approach applied to carbonate formations in north-western Iraq. Journal of Petroleum Science and Engineering, 196.

MOHAMMED-SAJED, O.K. and GLOVER, P.W.J., 2022. Influence of anhydritisation on the reservoir quality of the Butmah Formation in north-western Iraq. Marine and Petroleum Geology, 135.

NELSON, R., 2001. Geologic Analysis of Naturally Fractured Reservoirs. Gulf Professional Publishing, Massachusetts, USA.

OGILVIE, S.R., ISAKOV, E. and GLOVER, P.W.J., 2006. Fluid flow through rough fractures in rocks. II: A new matching model for rough rock fractures. Earth and Planetary Science Letters, 241(3-4), pp. 454-465.

OGILVIE, S.R., ISAKOV, E., TAYLOR, C.W. and GLOVER, P.W.J., 2003. Characterization of rough-walled fractures in crystalline rocks.

ORTEGA, O.J., MARRETT, R.A. and LAUBACH, S.E., 2006. A scale-independent approach to fracture intensity and average spacing measurement. American Association of Petroleum Geologists Bulletin, 90(2), pp. 193-208.

PANZA, E., AGOSTA, F., RUSTICHELLI, A., ZAMBRANO, M., TONDI, E., PROSSER, G., GIORGIONI, M. and JANISECK, J.M., 2016. Fracture stratigraphy and fluid flow properties of shallow-water, tight carbonates: The case study of the Murge Plateau (southern Italy). Marine and Petroleum Geology, 73, 350-370.

PHAM, C., CHANG, C., JANG, Y., KUTTY, A. and JEONG, J., 2020. Effect of faults and rock physical properties on in situ stress within highly heterogeneous carbonate reservoirs. Journal of Petroleum Science and Engineering, 185, 106601.

PRIOUL, R., DONALD, A., KOEPSELL, R., MARZOUKI, Z.E., BRATTON, T., 2007. Forward modeling of fracture-induced sonic anisotropy using a combination of borehole image and sonic logs. Geophysics 72 (4), 135–147.

RANJITH, P.G. and VIETE, D.R., 2011. Applicability of the 'cubic law' for non-Darcian fracture flow. Journal of Petroleum Science and Engineering, 78, 2, 321-327.

RASHID, F., 2008. Reservoir Characterizations of the Cretaceous Upper Qamchuqa Formation in Taq Taq Oil Field, Kurdistan Region, Northeast Iraq , MSc thesis, University of Sulaimani.

RASHID, F., GLOVER, P.W.J., LORINCZI, P., COLLIER, R. and LAWRENCE, J., 2015. Porosity and permeability of tight carbonate reservoir rocks in the north of Iraq. Journal of Petroleum Science and Engineering, 133, pp. 147-161.

RASHID, F. N., 2015. The Kometan formation: Reservoir characteristics of tight carbonates in the Western Zagros Basin. Ph.D. thesis, University of Leeds, Chapter 5, p. 166.

RASHID, F., HUSSEIN, D.O. and ZANGANA, H.A., 2020a. Petrophysical Investigation of the Khurmala Formation in Taq Taq Oil Field, Zagros Folded Belt. ARO-The Scientific Journal of Koya University, 8(1), 5-16.

RASHID, F., HUSSEIN, D., LAWRENCE, J. and KHANAQA, P., 2020b. Characterization and impact on reservoir quality of fractures in the Cretaceous Qamchuqa Formation, Zagros folded belt. Marine and Petroleum Geology, 113, 104-117.

RASHID, F., 2020. Reservoir Productivity Analysis of Intercalated limestone and Anhydrite Beds in Zagros Folded Belt, Kurdistan Region of Iraq. Kurdistan Journal of Applied Research, 5, 1, 1-15.

RASHID, F., HUSSEIN, D., LAWRENCE, J.A. and AHMED, Z., 2021. Fluid flow and permeability analysis of tight gas carbonate reservoir rocks using fractures and dynamic data. Journal of Natural Gas Science and Engineering, 90, 103894.

RASHID, F., HUSSEIN, D., GLOVER, P.W.J., LORINCZI, P. and LAWRENCE, J.A., 2022. Quantitative diagenesis: Methods for studying the evolution of the physical properties of tight carbonate reservoir rocks. Marine and Petroleum Geology, 139.

REIF, D., DECKER, K., GRASEMANN, B., and PERESSON , H., 2012. Fracture patterns in the Zagros fold-andthrust belt, Kurdistan Region of Iraq. Tectonophysics, 576-577, 46-62.

ROSALES, I., POMAR, L. and AL-AWWAD, S.F., 2018. Microfacies, diagenesis and oil emplacement of the Upper Jurassic Arab-D carbonate reservoir in an oil field in central Saudi Arabia (Khurais Complex). Marine and Petroleum Geology, Volume 96, Pages 551-576.

ROTEVATN, A. and BASTESEN, E., 2012. Fault linkage and damage zone architecture in tight carbonate rocks in the Suez Rift (Egypt): implications for permeability structure along segmented normal faults. Geological Society, London, Special Publications, 374, 79-95.

RUSHING, J. A., NEWSHAM, K. E., LASSWELL, P. M., COX, J. C., and BLASINGAME, T. A., 2004. Klinkenerg-Corrected Permeability Measurements in Tight Gas Sands: Steady-State Versus Unsteady-State Techniques. Society of Petroleum Engineers. doi:10.2118/89867-MS.

SHEN, J., QIN, Y., LI, Y., YANG, Y., JU, W., YANG, C. and WANG, G., 2018. In situ stress field in the FZ Block of Qinshui Basin, China: Implications for the permeability and coalbed methane production. Journal of Petroleum Science and Engineering, 170, 744-754.

SHENG, G., SU, Y. and WANG, W., 2019. A new fractal approach for describing induced-fracture porosity/permeability/ compressibility in stimulated unconventional reservoirs. Journal of Petroleum Science and Engineering, 179, 855-866.

SISSAKIAN, V.K., 2000. Geological Map of Iraq. Sheet No.1, scale 1: 1000 000, 3rd edition, GEOSURV, Baghdad, Iraq.

SKALINSKI, M. and KENTER, J., 2014. Carbonate petrophysical rock typing: Integrating geological attributes and petrophysical properties while linking with dynamic behaviour. Geological Society London Special Publications, 406, 1, 229-259.

TANIKAWA, W. and SHIMAMOTO, T, 2009. Comparison of Klinkenberg-corrected gas permeability and water permeability in sedimentary rocks. International Journal of Rock Mechanics and Mining Sciences, 46, 2, 229-238.

van BELLEN, R.C., DUNNINGTON, H.V., WETZEL, R. and MORTON, D.M., 1959. Iraq. In: Dubertret, L. (Ed.), Lexique Stratigraphique International, 3, Asie. CNRS, Paris fasc 10a, 333.

WENNBERG, O. P., SVÅNÅ, T., AZIZZADEH, M., AQRAWI, A. M. M., BROCKBANK, P., LYSLO, K. B. and OGILVIE, S., 2006. Fracture intensity vs. mechanical stratigraphy in platform top carbonates: the Aquitanian of the Asmari Formation, Khaviz Anticline, Zagros, SW Iran. Petroleum Geoscience, 12, 235-246.

WITHERSPOON, P.A., WANG, J.S., IWAI, K. and GALE, J.E., 1980. Validity of cubic law for fluid flow in a deformable rock fracture. Water Resources Research, 16, 6, 1016-1024.

WU, G., ZHAO, K., QU, H., SCARSELLI, N., ZHANG, Y., HAN, J. and XU, Y. 2020. Permeability distribution and scaling in multi-stages carbonate damage zones: Insight from strike-slip fault zones in the Tarim Basin, NW China. Marine and Petroleum Geology, 114, 104208.

YALE, D.P., 2003. Fault and stress magnitude controls on variations in the orientation of in situ stress. Geological Society London, Special Publication, 209, 1, 55-64.

YU, P., LIU, Y., WANG, J., KONG, C., GU, W., XUE, L., CHENG, Z. and JIANG, L., 2020. A new fracture permeability model: Influence of surrounding rocks and matrix pressure. Journal of Petroleum Science and Engineering, 193, 107320.

YUE, D., WU, S., XU, Z., XIONG, L., CHEN, D., JI, Y. and ZHOU, Y., 2018. Reservoir quality, natural fractures, and gas productivity of upper Triassic Xujiahe tight gas sandstones in western Sichuan Basin, China. Marine and Petroleum Geology, 89, 2, 370-386.

ZHANG, Y., ZHANG, J., YUAN, B. and YIN, S., 2018. In-situ stresses controlling hydraulic fracture propagation and fracture breakdown pressure. Journal of Petroleum Science and Engineering, 164, 164-173.

List of figures

Figure 1. Geological map of the Kurdistan region of northern Iraq showing the location of the Taq Taq field and the studied wells (modified after Sissakian, 2000; Rashid et al., 2020b). The inset box shows the terrain border of Iraq, and the red rectangle therein represents the location of the geologic map of northern part of Iraq. See Figure 3 for the geological age and lithology of stratigraphic units.

Figure 2. Structure map of the Taq Taq anticline with depth contours (m) on the top of the Shiranish Formation. Dots show the locations of the three wells studied: TT-05 on the crest of the structure, and TT-06 and TT-07 on the flanks. The location of this map is presented in the red rectangle in Figure 1.

Figure 3. Lithostratigraphic chart for the Taq Taq structure; lithologies are based on core descriptions, cuttings identification and wireline log analyses from the drilled wells .

Figure 4. Interpreted NE-SW seismic cross-section of the Taq Taq anticline. The thrust fault bounding the SW of the structure terminates within the Eocene Pilaspi Formation, and the back thrust at the NE flank terminates within the Kolosh Formation.

Figure 5. Fracture types in cores of limestone and argillaceous limestone from the Shiranish Formation. A: Sub-vertical partly open fracture with aperture greater than 0.10 mm (macro-fracture), Core 1, depth 1916.61 m, Well TT-05. B: Sub-vertical open fracture with an aperture of 2-3 mm, Core 1, depth 1924.35m, Well TT-05. C: Fault breccia, the fault is filled with white saddle dolomite and contains oil stain, Core 2, depth 1956.30 m, Well TT-05. D: Fault breccia, the fault surface is filled with calcite and saddle dolomite, Core 2, depth 1956.95 m, Well TT-05.

Figure 6. A simple schematic of a fracture in order to define the three fracture parameters used in this work. The fracture is shown as irregular as the core data indicated that this was invariably true. The figure shows no cementation, but where cementation was noted, the fracture dimensions were measured assuming that it was not present.

Figure 7. Lithostratigraphic columns for the Upper Cretaceous Shiranish Formation at wells TT-06, TT-05 and TT-07 (locations in Figure 2) together with gamma log profiles (and LLD and LLS profile for well

TT-05). Lithological variations were obtained from descriptions of core and cuttings samples, as well as from petrophysical and lithological logs.

Figure 8. Photomicrographs in plane polarised light of Shiranish Formation samples from the Taq Taq field. A: Argillaceous lime mudstone with benthic and planktonic foraminifera, depth 1831m, Well TT-04.B: Argillaceous packstone with glauconite grains, depth 1942m, Well TT-06. C: Wackestone with abundant planktonic foraminifera whose chambers are filled with ferroan calcite, depth 1915m, Well TT-05. D: Wackestone crossed by cemented fracture, cemented fracture showing multiple opening and calcite filling with fracture pores, depth 1921m, Well TT-05.

Figure 9. Histograms of the frequency of occurrence for various properties of fracture expressed as a percent of the total dataset. (A) Fracture aperture (mm) for observed fractures in core samples of the Shiranish Formation, including natural open fractures and partly mineralised fractures. (B) Fracture length for observed fractures measured in both open and partly open fractures in core samples (non-linear bin). (C) Fracture height of naturally formed open and partially open fractures in core samples (non-linear bin).

Figure 10. Orientation of fractures and micro-faults presented on upper hemisphere Schmidt Stereonet pole plots, rose diagrams and frequency dip angles. Fracture orientations were collected from core samples and XRMI micro-resistivity image logs from wells TT-05, TT-06 and TT-07.

Figure 11. Fracture types observed on XRMI micro-resistivity image logs of the studied wells. The images were picked from different intervals to illustrate fractures based on resistivity contrasts.

Figure 12. Histograms of porosity and permeability. A: Histogram of measured matrix porosity and calculated fracture porosity in the Shiranish Formation. B: Histogram of the measured Klinkenberg-corrected matrix permeability and calculated fracture permeability from the available core samples.

Figure 13. Cross-plots of fracture permeability (mD) as a function of confining pressure (0 - 4000 psi) for selected core samples from the Shiranish Formation. Permeabilities range across four orders of magnitude from 1 to 1000 mD for zero confining pressure. (A) Sample has 5.2 mD measured permeability at zero confining pressure. (B) Sample has 50.7 mD measured permeability at zero confining pressure. (C) Sample has 389.3 mD measured permeability at zero confining pressure. (D) Sample has 4046 mD measured permeability at zero confining pressure.

Figure 14. Profiles of frequency versus depth of natural open and partially mineralised fractures obtained from the micro-resistivity borehole images and available core samples of the Shiranish Formation from wells TT-07, TT-05 and TT-06. The fracture frequency for the lower part of the formation in Well TT-05 is presented by numbers for scale adjustment purposes only. This data is also shown in Figures 9, 10 and 16 and in abstracted form in other figures.

Figure 15. Cross-plot of the calculated fracture porosity (ϕ) versus fracture permeability (k) for core plug samples from the Shiranish Formation. The Figure shows that the porosity and permeability distribution can be grouped into two principal hydraulic flow units, HFU1 and HFU2.

Figure 16. Profiles versus depth of fracture permeability and fracture parameters including frequency, aperture, height and lengths as measured in cores C1 and C2 of the Shiranish Formation in Well TT-05. Both the core and the image logs were checked for depths where a correlation between enhanced permeability and fracture size parameters was indicated. There was evidence for good correlation in the six depth ranges shown as grey boxes.

Figure 17. (a) Permeability (k in mD) as a function of fracture aperture (A in mm) for 18 core plug samples, together with theoretical curves showing the best fit Hagen-Poiseuille law (blue, R^2=0.9884), the lower bound (read) and the upper bound (green). (b) The same permeability values (now in m^2) plotted as a function of aperture cubed (now in m^3) on double logarithmic scales, with the same theoretical curves as in Part (a).

Figure 18. Modelled rough fracture surfaces using Synfrac© using the same parameters as the Hachimantai test site (Glover et al., 1998) as an indication of the roughness expected in Shiranish fractures. The figure shows a map of the top surface of the fracture together with two cross-sections showing the top and bottom profiles as well as the modelled fracture parameters. Please see the figure for the specific fracture properties.

List of tables